POLITECNICO DI TORINO
Repository ISTITUZIONALE

On the aeroacoustics of a propeller at low Reynolds number subjected to a grid-induced turbulent inflow

*Original*
On the aeroacoustics of a propeller at low Reynolds number subjected to a grid-induced turbulent inflow / Ali, M., Piccolo, A., Zamponi, R., Ragni, D., Avallone, F.. - In: AEROSPACE SCIENCE AND TECHNOLOGY. - ISSN 1270-9638. - 176, Part A:(2026). [10.1016/j.ast.2026.112114]

*Availability:*
This version is available at: 11583/3008794 since: 2026-03-16T09:25:38Z

*Publisher:*
Elsevier

*Published*
DOI:10.1016/j.ast.2026.112114

*Terms of use:*

This article is made available under terms and conditions as specified in the corresponding bibliographic description in the repository

*Publisher copyright*

(Article begins on next page)

08 November 2026

Aerospace Science and Technology 176 (2026) 112114

Contents lists available at ScienceDirect

Aerospace Science and Technology

journal homepage: www.elsevier.com/locate/aescte

Original article

# On the aeroacoustics of a propeller at low Reynolds number subjected to a grid-induced turbulent inflow

Mario Alì [a,*], Andrea Piccolo [b], Riccardo Zamponi [b,c], Daniele Ragni [b], Francesco Avallone [a]

[a] Politecnico di Torino, Corso Duca degli Abruzzi, 24, Torino, 10129, Italy
[b] Delft University of Technology, Kluyverweg 1, Delft, 2629 HS, The Netherlands
[c] von Karman Institute for Fluid Dynamics, Waterloosesteenweg 72, Sint-Genesius-Rode, B-1640, Belgium

ARTICLE INFO

Dr Qu Qiulin

*Keywords:*
Propeller
Turbulence ingestion noise
Turbulence distortion
Inflow inhomogeneity
Laminar separation bubble

ABSTRACT

This work investigates the effect of grid-generated turbulence ingestion on noise generation in a propeller operating at a low Reynolds number using high-fidelity, scale-resolved simulations. The numerical setup reproduces experiments carried out at Delft University of Technology, where inflow turbulence is generated by a grid placed within a duct. It is found that, upstream of the propeller, the longitudinal correlation length of the streamwise velocity component increases with respect to the case without the propeller. The opposite happens for the transversal one. The turbulent inflow impinging on the propeller blades does not alter the mean flow characteristics over the propeller blades, e.g., the mean static pressure coefficient. However, it increases the root mean square of the pressure fluctuations up to the turbulent reattachment point of the laminar separation bubble, while leaving the downstream region mostly unaffected. This causes a broadband increase in the radiated noise in the low-to-mid frequency range, as confirmed by applying Amiet's noise-prediction model with input data sampled near the propeller blades' leading edge. The far-field noise spectra are characterized not only by an increase in the broadband noise with respect to the clean inflow case, but also by tonal components at multiples of the blade-passing frequency. It is found that these tones are caused by the footprint of the turbulence grid that introduces flow inhomogeneities at the propeller location for this specific configuration. It is recommended, when performing experiments and simulations, to verify if any footprint of the turbulence grid is present, not only by performing single-point measurements but also by measuring the time-averaged flow field before installing the propeller.

## 1. Introduction

The interaction between a turbulent flow and rotating blades is a phenomenon encountered in numerous engineering applications, such as wind turbines [1], aircraft engines [2], helicopter rotors [3], and submarine propellers [4]. In all these cases, inflow velocity fluctuations give rise to unsteady surface pressure and, consequently, unsteady loading [5].

The rapid growth in the use of small Unmanned Aerial Vehicles (UAVs) [6], driven by diverse applications such as goods delivery and urban air mobility [7], has introduced specific challenges to their integration into urban environments [8,9]. Among these, the acoustic footprint of small propellers plays a critical role in public acceptance [10], underscoring the need for a comprehensive understanding of their aerodynamic and aeroacoustic behavior under complex urban turbulence conditions, influenced by atmospheric boundary layer effects and upstream obstacles [11].

Small UAV propellers typically operate at low Reynolds numbers, placing them in a transitional flow regime that is highly sensitive to inflow turbulence and marked by complex aerodynamic phenomena such as Laminar Separation Bubbles (LSB), flow reattachment, and transition to turbulence [12]. The rotation of these blades generates both tonal and broadband noise components [13]. For thin blades operating at low Mach numbers, the dominant acoustic sources are steady and unsteady aerodynamic loads [14,15]. Tonal noise associated with steady loading arises due to the periodic variation in the orientation of the loading vector as the blade rotates, which appears unsteady in the inertial frame [15]. In contrast, unsteady loading results directly from fluctuations in surface pressure, typically induced by leading-edge interactions with incoming turbulence, laminar separation on the suction

* Corresponding author.
*E-mail address:* mario.ali@polito.it (M. Alì).

https://doi.org/10.1016/j.ast.2026.112114
Received 17 December 2025; Received in revised form 4 February 2026; Accepted 10 March 2026
Available online 15 March 2026
1270-9638/© 2026 The Author(s). Published by Elsevier Masson SAS. This is an open access article under the CC BY license (http://creativecommons.org/licenses/by/4.0/).

or pressure sides, reattachment, transition, or trailing-edge scattering [12].

The LSB influences high-frequency noise by affecting boundary-layer transition [12,16] or by generating coherent Tollmien–Schlichting waves [17]. Numerous studies have examined the dynamics of the LSB in steady two-dimensional airfoils. For instance, the dependence of the LSB on the angle of attack, the Reynolds number, and the airfoil geometry has been demonstrated [18,19]. As the angle of attack increases, the LSB shifts toward the leading edge due to the stronger adverse pressure gradient, eventually bursting near the leading edge. The effect of the Reynolds number on the LSB of a NACA 0012 airfoil, over the range $0.5 \times 10^5$ to $4 \times 10^5$, has been investigated numerically [20]. At low Reynolds numbers, large coherent structures are shed from the LSB on the suction side and convected over the trailing edge. As the Reynolds number increases, the flow transitions to a fully turbulent regime, reducing the size of the coherent structures and causing the LSB to nearly vanish. In this regime, only small turbulent eddies are convected over the trailing edge. The influence of Free-Stream Turbulence (FST) intensity and the streamwise integral length scale on the formation and development of an LSB has also been explored [21]. Elevated FST levels were found to advance the transition and reduce bubble size, with complete elimination at the highest turbulence intensities. Moreover, for a fixed turbulence intensity, the integral length scale was shown to play a negligible role.

The LSB has also been observed experimentally on a small propeller operating at a tip Reynolds number of $Re_{tip} \approx 3.5 \times 10^4$, across advance ratios $J$ ranging from 0 to 0.6 under clean inflow conditions [22]. Oil-flow visualizations revealed that the LSB shifted toward the leading edge and decreased in size as the advance ratio decreased, owing to the higher angle of attack. Variations in the position of the turbulent reattachment point influence the development of the downstream turbulent boundary layer, thus affecting high-frequency components in the acoustic spectra. A numerical study on the same propeller, performed at 4000 and 5000 rpm for an advance ratio of $J = 0.6$, confirmed that both the size and position of the LSB are primarily governed by the advance ratio, with negligible influence from the rotational speed [12].

Concerning the impact of turbulence on the LSB in rotors, only a limited number of studies are available. The effects of flow confinement on propeller acoustics were investigated for $J = 0$ and 0.6 [16]. Under ascending flight conditions ($J = 0.6$), the inflow was clean, whereas under hovering conditions ($J = 0$), the recirculating flow within the anechoic chamber was ingested into the propeller plane. Few differences were observed in the higher-order tones of the acoustic spectrum between the confined and unconfined cases. Free-stream turbulence has also been shown to enhance the aerodynamic performance of low-Reynolds-number propellers, primarily through suppression of laminar separation and earlier transition [23]. Such a suppression should, in turn, reduce trailing-edge noise, as demonstrated for tripped transition on airfoils [24]. Furthermore, the aeroacoustic characteristics of a propeller subjected to grid-generated turbulence have been documented [25]. Compared with the clean inflow case, ingested turbulence was found to introduce tones in the mid-frequency range, elevate the broadband noise floor, and increase Sound Pressure Levels (SPL) for the first few tones and across the high-frequency range.

Given the acoustic relevance of turbulence ingestion, several studies have focused on developing low-order models to predict the resulting noise. Early work showed that the broadband noise generated by a rotor in a turbulent inflow depends on the turbulence intensity, the integral length scale, and the rotor radius [26]. By combining the incoming turbulence spectrum with the two-dimensional aerodynamic response function of an airfoil, the spectrum of the normal axial force acting on the rotor was computed and the broadband component of the acoustic spectrum was estimated assuming dipole radiation. Although this method provided good agreement for the broadband contribution, it failed to capture the quasi-tonal content of the spectrum. This quasi-tonal component was later attributed to the streamwise elongation of the eddies caused by rotor-induced streamtube contraction [27]. Specifically, the ratio of longitudinal to transverse integral length scales was found to increase strongly, indicating that, even if turbulence is isotropic far upstream, it becomes anisotropic near the propeller due to the distortion. These elongated eddies, repeatedly chopped by the rotor, produced partially coherent unsteady loading over the blades (*blade-to-blade correlation*), which manifested as quasi-tonal noise around the Blade-Passing Frequency (BPF) harmonics (*haystacking*). This noise source arises when the passage time of the largest eddies through the propeller plane exceeds the time between successive blade passages [15]. This hypothesis was confirmed by introducing the blade-to-blade correlation into predictive models, which successfully recovered the quasi-tonal content [28]. Experiments further showed that increasing the turbulence integral length scale did not increase the overall SPL, whereas higher turbulence intensity elevated the broadband noise floor, with only the lower BPF harmonics increasing by about 2 dB [29].

Amiet extended his prediction model for rectilinear motion [30] to rotating blades by approximating circular motion as rectilinear in the limit of acoustic frequencies much higher than the rotational frequency ($\omega \gg \Omega$) [31]. The model relates the acoustic spectrum to the characteristics of incoming turbulence via an acoustic transfer function, under the assumptions of frozen turbulence, a blade profile assimilated to a flat plate at zero angle of attack, and infinite span. Consequently, turbulence distortion induced by the mean flow field is not taken into account. Validation against helicopter rotor data showed that the model tends to underestimate noise at angular positions close to the rotor plane, while at far-field positions it provides good agreement in the mid-frequency tonal range but overpredicts low-frequency quasi-tonal noise [3]. More recent studies have refined the model. A corrected formulation of the eddy chopping time improved the prediction of the acoustic spectrum and showed that haystacking is underestimated when the turbulence integral length scale is large relative to the blade radius, due to the neglect of the spanwise correlation in the direct strip approach [32]. Extensions have also been developed to account for spanwise-varying flow conditions in rectilinear motion, including an inverse strip approach that recovers spanwise correlation [33]. More recently, [34] proposed a reformulation of Amiet's model using only the upwash velocity spectrum as input to acoustic prediction.

The studies reviewed above do not explicitly examine the impact of turbulence distortion on noise prediction for a rotating blade. Turbulence distortion alters the spectrum of upwash velocity fluctuations, thereby modifying the noise generation mechanism. In the case of airfoils, this phenomenon is well documented. A large body of work characterizes turbulence–airfoil interaction [35–37], with modifications of both the turbulence spectrum [38] and the aeroacoustic transfer function [36,39] proposed to account for it. In particular, modifications of the turbulence spectrum are often based on the Rapid Distortion Theory (RDT) [40], a linearized framework that assumes small fluctuations and inviscid mean flow to compute the properties of turbulence along the stagnation line in front of a bluff body.

The objective of this paper is to investigate how grid-generated turbulence is modified when interacting with a propeller, how it affects the flow development over the blades, and therefore impacts the noise sources and the far-field noise. While these aspects have been investigated experimentally [25,34,41], numerical studies have been carried out only on the interaction of a cylinder wake with a propeller [42], to mimic large-scale structures, and not with grid-generated turbulence for smaller-scale turbulent structures as often done in the experiments. The inherent limitations of experimental studies hinder a detailed source identification and blade-level analysis. To overcome these constraints, a numerical tool is employed to enable a comprehensive investigation of the interaction with impinging turbulence. Furthermore, the present study can provide high-fidelity data on the effects of inflow turbulence on broadband and tonal noise at low Reynolds numbers, supporting the validation and extension of noise prediction models for UAV propellers. To this end, three numerical setups were implemented in PowerFLOW

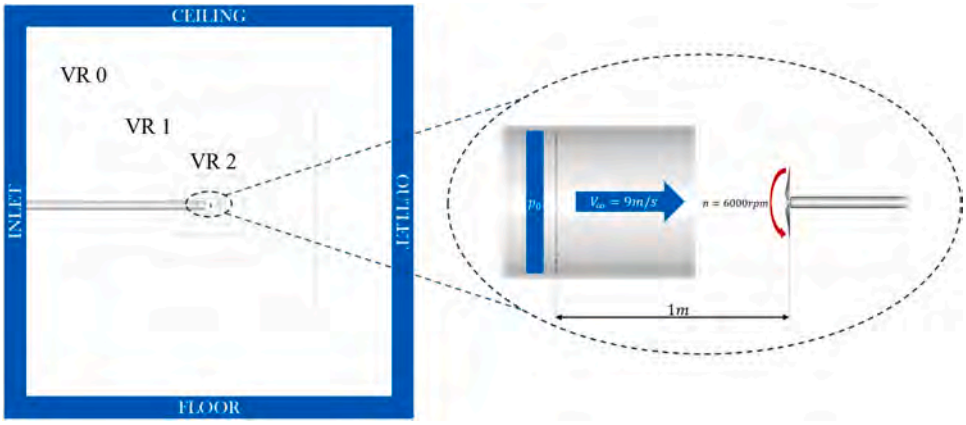


**Fig. 1.** Numerical domain: left, complete domain with far-field boundary conditions; right, detailed view of the region of interest, featuring the duct, grid, propeller, and the boundary condition where $p^0$ is prescribed.

6-2022-R1: a free turbulent jet, a propeller subjected to grid-generated turbulent inflow, and a propeller operating under clean inflow conditions. These configurations replicate experimental measurements carried out at TU Delft, also used for validating the simulation. The comparison between the free-jet case and the one with the propeller in the presence of turbulent inflow enables the description of how the incoming turbulence is affected by the propeller's presence. In contrast, the comparison between the clean-inflow case and the turbulent-inflow one in the presence of the propeller is used to describe how turbulence alters the aerodynamic and acoustic fields.

The paper is organized as follows: the numerical setup is described in Section 2.2 and validated in Section 2.3. Section 3 presents the study findings and is organized as follows. It starts with a qualitative description of the flow field around the propeller in Subsection 3.1. The turbulent inflow is then characterized in the absolute reference frame (Subsection 3.2) and in the local rotating frame near the blade leading edge (Subsection 3.3). The analysis subsequently examines the impact of the turbulent interaction on the flow development over the blade surface in Subsection 3.4. The resulting effects on acoustics and noise sources are discussed in Subsection 3.5. Finally, Subsection 3.6 employs Amiet's model to quantify the combined effects of turbulence and flow inhomogeneity on the acoustic response. The main conclusions are summarized in Section 4.

## 2. Methodology

### 2.1. Computational method

The software PowerFLOW 6-2022-R1 is used to compute the flow field and extract the data required by the [14] analogy (FW-H) to retrieve the acoustic field. The software is based on the Lattice-Boltzmann Method (LBM). Here, the only unknown quantity is the particle Probability Distribution Function (PDF) $f(\mathbf{x}, t, \mathbf{v})$, which represents the probability that a particle in location $\mathbf{x}$ and instant $t$ has a velocity $\mathbf{v}$ [43]. The evolution of the particle PDF is described by the Boltzmann equation, which relies on gas-kinetic theory.

The discrete Boltzmann equation

$$f_i(\mathbf{x} + \mathbf{v}_i dt, t + dt) - f_i(\mathbf{x}, t) = C_i(\mathbf{x}, t) \tag{1}$$

is solved on a Cartesian mesh called lattice, whose base elements are called voxels. The size of the voxels halves from a resolution region to the next finer one. The regions where the size of the voxel is constant are called Variable Resolution (VR). Macroscopic quantities are retrieved from the statistical moments of $f$ [44]. The source term on the right-hand side is the so-called collision term. It includes the interaction among particles in the evolution of $f$ toward thermodynamic equilibrium.

In PowerFLOW, the Bhatnagar–Gross–Krook (BGK) operator is adopted, which ensures the conservation of mass, momentum, and energy [45]:

$$C_i(\mathbf{x}, t) = -\frac{\Delta t}{\tau}(f(\mathbf{x}, t) - f^{eq}(\mathbf{x}, t)). \tag{2}$$

Here, $\tau$ is the relaxation time and $f^{eq}$ is the local Maxwell-Boltzmann equilibrium distribution. In the traditional formulation, the relaxation time is given by the sum of a viscous and a turbulent term:

$$\tau_{\text{eff}} = \tau_{\text{visc}} + \tau_{\text{turb}} = \tau_{\text{visc}} + C_\mu \frac{k^2/\epsilon}{T\sqrt{1+\eta^2}}, \tag{3}$$

where $C_\mu = 0.09$, $k$ and $\epsilon$ are turbulent kinetic energy and dissipation, respectively, and $\eta$ is a function of local strain, vorticity, and helicity. This study uses a formulation of the relaxation time $\tau_{\text{eff}}$ that excludes the turbulent term. In this formulation, called Implicit Large Eddy Simulation LBM (ILES - LBM), the inviscid energy cascade through the inertial range is captured by the numerical scheme, and the inherent numerical dissipation acts as a sub-grid model [46]. This strategy allows for a reduction in eddy viscosity and enables the capture of the LSB [12]. In addition, since reaching a $y^+$ lower than 1 in a Cartesian mesh would be computationally prohibitive for the case study, a fully turbulent wall function model, extended to include the effects of pressure gradient, is applied on the propeller surface [47].

### 2.2. Numerical setup

In the following, $x$, $y$ denote the streamwise and radial directions, respectively, while $u$ represents the streamwise velocity component, normal to the rotational plane. The origin of the coordinate system is at the hub.

The computational domain is a cube with a side length of $100D_{\text{prop}}$, where $D_{\text{prop}} = 30\,\text{cm}$ denotes the propeller diameter. Both the turbulence grid and the propeller are located at the center of the domain (Fig. 1). The domain is discretized into 17 VRs (numbered 0–16) with progressively finer resolution toward the propeller. VR11 extends from the grid to two diameters downstream of the propeller plane, enclosing the nacelle, with a voxel size of 0.88 mm.

Five additional inner VR levels (VR12–16) are defined around the propeller using blade-offset refinements (Fig. 2). This allows achieving a maximum $y^+ \approx 4$, sufficient to resolve the LSB on the suction side of the blades [12,16,47]. The complete mesh contains approximately $1.2 \times 10^9$ voxels, with a minimum voxel size of 0.03 mm.

The numerical setup, shown in Fig. 3, reproduces the reference experimental configuration [34,48]. Air enters the domain through a cylindrical tube of diameter $D = 0.6\,\text{m}$ with frictionless walls, at a velocity of $V_\infty = 9\,\text{m s}^{-1}$. A turbulence grid with mesh size $M = 0.1\,\text{m}$ is placed into

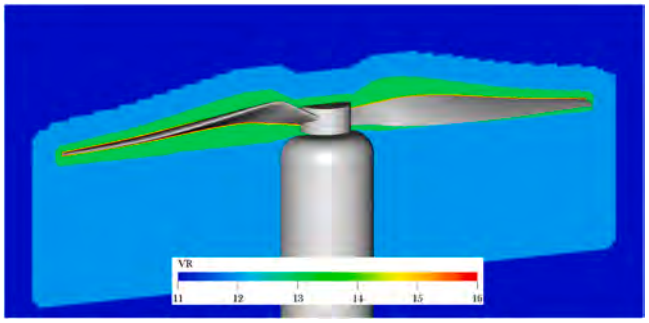


**Fig. 2.** Near-body mesh. VR11 (external) resolves incoming turbulence, while inner VRs (VR12–16) refine the propeller region.

the tube, at 0.6 m from the exit. The propeller plane is located at 1 m (10 $M$) downstream of the grid. This distance, which is the same as that used in the experiments, does not allow for a fully developed and homogeneous inflow as discussed in Section 3.

The propeller, also used in previous studies [12,22], has a diameter $D_{\text{prop}} = 0.3$ m and features a NACA-4412 airfoil as blade section along the entire span. It rotates at $n = 6000$ rpm, corresponding to an advance ratio $J = V_\infty/(nD_{\text{prop}}) = 0.3$.

A total pressure $p_0 = 101\,399$ Pa is prescribed upstream of the grid to match the reference mean velocity while accounting for local pressure losses $\Delta p^0$ induced by the grid, computed following [49]:

$$\frac{\Delta p^0}{q} = A\left(\frac{1}{\beta^2} - 1\right)^B, \tag{4}$$

where $q$ is the dynamic pressure, $\beta$ the grid porosity, and $A$ and $B$ are functions of Reynolds number, Mach number, and grid geometry. For a square-mesh grid, $\beta$ is given by:

$$\beta = \left(1 - \frac{d}{M}\right)^2. \tag{5}$$

Free-stream velocity and ambient static pressure are imposed at the domain boundaries. Twenty probes upstream of the propeller are used to characterize the inflow (Fig. 3), sampled over 10 revolutions at $f_s = 20$ kHz. The turbulence spectrum is obtained via Welch's method using four overlapping blocks (50 %) and a frequency resolution of $\Delta f = 20$ Hz.

Far-field noise is predicted using the time-domain FW-H analogy in its solid formulation, based on Farassat 1A [50,51]. Surface pressure is sampled over the propeller at $f_s = 367$ kHz with a spatial averaging of 0.4 mm. Quadrupole contributions are neglected because of the low wake Mach number [15]. The acoustic propagation to microphone locations is performed in the solver PowerACOUSTICS.

The fine-resolution simulation required $2.07 \times 10^5$ CPU-hours. The simulated physical time covers 13 propeller revolutions, with data acquisition starting after three initial settling revolutions. Clean inflow simulations were conducted by removing the turbulence grid and resetting $p^0$. VR11, previously used to resolve incoming turbulence, was restricted to a propeller offset, preserving local resolution while reducing computational cost.

Due to the high computational cost associated with the high spatial resolution needed to capture the relevant flow physics over the propeller and the resulting small timestep, the present study is limited to a single turbulent inflow realization and one inflow velocity. However, it is worth mentioning that [25] experimentally investigated the effects of two grid-generated turbulence conditions on the aeroacoustics of a small propeller, with turbulence intensities of 4.9% and 10.1% and corresponding integral length scales of 1.3mm and 1.9mm. The resulting acoustic spectra exhibited similar trends for both turbulent cases. In addition, they investigated the effects of varying the inflow velocity while keeping the rotational speed constant, and observed similar trends in the mid-frequency region of the acoustic spectra. Based on these considerations, the results of the current study can be considered generalizable.

### 2.3. Validation

In the following, $(\cdot)'$ denotes the fluctuating component of a quantity, while $\overline{(\cdot)}$ indicates time averaging. Grid convergence was assessed for all cases and validated against reference experimental data [34,48]. Three mesh resolutions were considered: coarse, medium, and fine. The characteristic grid length $M$ was discretized with 80 and 120 voxels at the coarse and medium levels, respectively, with four inner VRs around the propeller. The fine mesh includes an additional VR to locally refine the propeller region while maintaining the inflow turbulence resolution of the medium case.

Since a load cell was not used in the experiment, the numerical thrust and torque coefficients

$$C_T = \frac{T}{\rho n^2 D^4}, \qquad C_Q = \frac{Q}{\rho n^2 D^5} \tag{6}$$

were compared with literature values obtained using a BEMT approach [12]. The results, reported in Table 1, show good agreement for both $C_T$ and $C_Q$.

Flow quantities at $x/R = -1$ and $y/R = 0.5$, without and with the propeller, are summarized in Table 2. To correctly compare the experimental hot-wire measurements with the numerical virtual probes, the mean velocity and turbulence intensity were computed following [52]:

$$V_{\text{mean}} = \sqrt{\overline{u}^2 + \overline{v}^2}, \qquad \text{TI} = \frac{\sqrt{(u'\cos\alpha)^2 + (v'\sin\alpha)^2}}{V_{\text{mean}}}, \tag{7}$$

where $u$ and $v$ are the streamwise and normal velocity components, respectively, and $\alpha$ is defined as:

$$\alpha = \arctan\left(\frac{v}{u}\right). \tag{8}$$

The integral time scale $T_{uu}$ was obtained from the autocorrelation function as:

$$T_{uu} = \int_0^{\tau_f} \chi_{uu}(\tau)\,\mathrm{d}\tau = \int_0^{\tau_f} \frac{\overline{u'(t)u'(t+\tau)}}{\overline{u'(t)u'(t)}}\,\mathrm{d}\tau, \tag{9}$$

with the upper limit $\tau_f$ corresponding to the point where $\chi_{uu}$ decreases to $1/e^2$ from its maximum. In the simulations including the propeller, the phase-locked average was subtracted to remove the periodicity induced by blade passage, isolating the broadband turbulent inflow component [17,53].

The integral time scale is reported instead of the integral length scale, as axial velocity gradients induced by the propeller invalidate Taylor's frozen-turbulence assumption. Numerical and experimental results show satisfactory agreement, with numerical $V_{\text{mean}}$ being up to 0.6 m s$^{-1}$ higher than the measured one.

The turbulence spectra of the streamwise component $u$ at $x/R = -1$ and $y/R = 0.5$ are shown in Fig. 4. Good agreement is observed in the resolved frequency range. The spectrum for the medium-resolution case is not shown, since the resolution of the turbulent inflow is identical to that of the fine case. The drop from the 6$^{\text{th}}$ and 8$^{\text{th}}$ BPF harmonics for the coarse and fine mesh, respectively, is due to the mesh filter effect: at least 10 voxels per wavelength are needed to prevent numerical dissipation. While increasing resolution would capture up to the 10$^{\text{th}}$ BPF harmonic, the computational cost would become prohibitive.

Time-averaged surface streamlines and oil-flow visualizations under turbulent and clean inflow conditions are compared in Fig. 5. Both separation and transition points are slightly delayed in comparison with the experiments, likely due to the higher mean inflow velocity (reducing the local angle of attack) and to the wall modeling approach used. The influence of wall models on the LSB prediction will be addressed in future work.

Acoustic spectra at microphones 1 and 4, with reference pressure $p_{ref} = 2 \times 10^{-5}$ Pa, are reported in Fig. 6 for all mesh resolutions. Both turbulent and clean inflow cases show excellent agreement for the first two BPF harmonics, dominated by steady loading and thickness noise

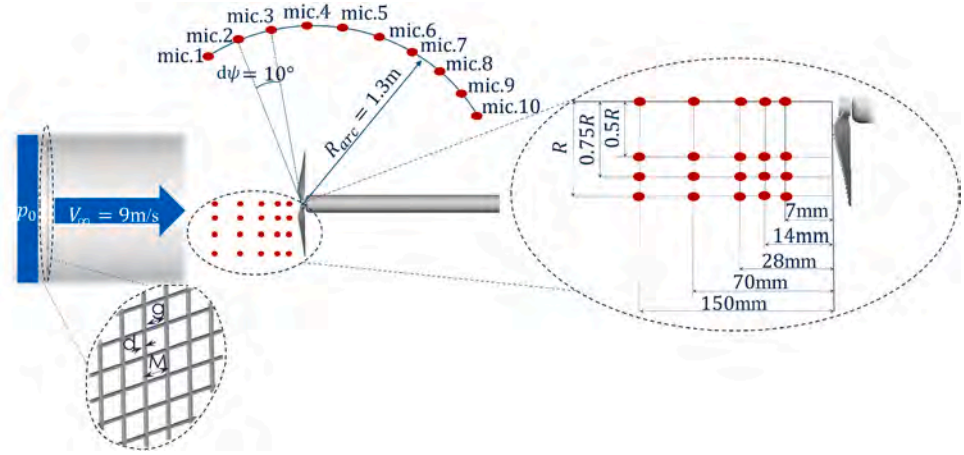


**Fig. 3.** Numerical setup. The characteristic sizes of the grid are: $g = 9 \times 10^{-2}$ m, $d = 1 \times 10^{-2}$ m and $M = 1 \times 10^{-1}$ m. The red points in the zoomed region on the right identify the probes used to characterize the inflow, while the ones distributed along the arc identify the location of the microphones. For interpretation of the references to colour in this figure legend, the reader is referred to the web version of this article.

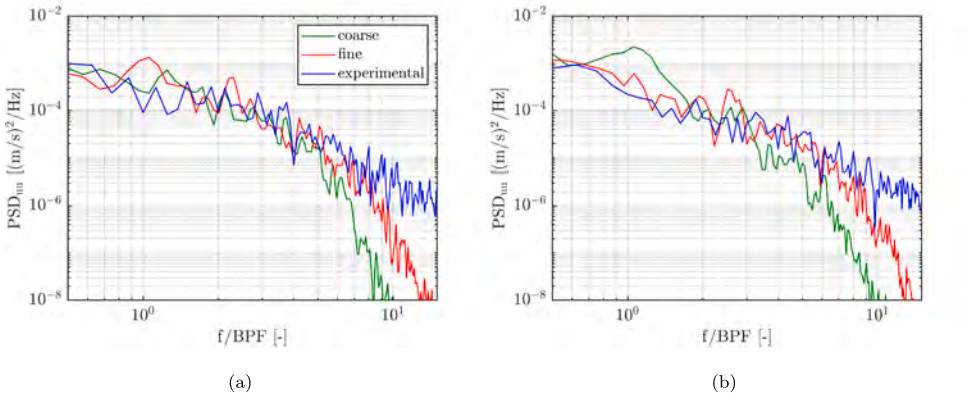


**Fig. 4.** Convergence of the turbulence spectrum at $x/R = -1$ and $y/R = 0.5$ (a) without and (b) with propeller. The spectrum for the medium-resolution case is not shown, as the resolution of the turbulent inflow is identical to that of the fine case.

**Table 1**
Convergence of $C_T$ and $C_Q$.

| | Coarse | Medium | Fine | BEMT [12] |
|---|---|---|---|---|
| $C_T$ | 0.087 | 0.088 | 0.093 | 0.09 |
| $C_Q$ | 0.008 | 0.0081 | 0.0078 | 0.008 |

**Table 2**
Flow quantities extracted at $x/R = -1$ and $y/R = 0.5$.

| | $V_{mean}$ [m s$^{-1}$] | | TI [%] | | $T_{uu}$ [s] | |
|---|---|---|---|---|---|---|
| | Exp. | Num. | Exp. | Num. | Exp. | Num. |
| wo prop. | 9 | 9.52 | 6.41 | 6.84 | 0.0017 | 0.0026 |
| w prop. | 9.68 | 10.33 | 5.6 | 5.59 | 0.002 | 0.0016 |

[54,55]. Differences at higher frequencies (f/BPF > 50 up to 5 dB) are attributed to variations in flow reattachment and turbulent boundary layer interaction with the trailing edge. In the experiments, motor noise dominates the third harmonic. The experimental half-BPF harmonics are due to the loaded electric motor noise and the non-perfect balance of the blade loading [12]. The maximum deviation in the first two harmonics is below 2 dB, consistent with the slightly higher mean velocity in the simulations. At the microphones located in the propeller plane (Fig. 6 (b,d)), a discrepancy is observed between the numerical results and the experimental data. A similar mismatch at this location has also been reported in previous studies [12,16] where it was attributed to electric motor noise. Overall, the numerical predictions show only minor deviations from the experiments, confirming the validity of the computational approach.

## 3. Results and discussion

The description and discussion of the results follow the structure outlined below. First, a qualitative overview of the flow around the propeller is presented in Section 3.1. Next, a detailed characterization of the incoming flow is provided in both the absolute (Section 3.2) and local (Section 3.3) frames of reference. This is done to assess the impact of both the streamtube contraction and the leading-edge-induced distortion on the ingested turbulence. The effects of the inflow turbulence on the propeller aerodynamics are then examined in Section 3.4. Finally, the acoustic results are discussed and connected to the aerodynamic sources in Section 3.5.

### 3.1. Description of the flow around the propeller

Fig. 7 shows an instantaneous snapshot of the Turbulent Kinetic Energy (TKE), defined as

$$\mathrm{TKE} = \frac{1}{2}\left((u')^2 + (v')^2 + (w')^2\right) \tag{10}$$

at the propeller mid-plane for both the turbulent (Fig. 7a) and clean (Fig. 7b) cases. The visualization highlights ingested turbulence, tip vortices, and downstream wake. In the turbulent inflow case (Fig. 7a), only

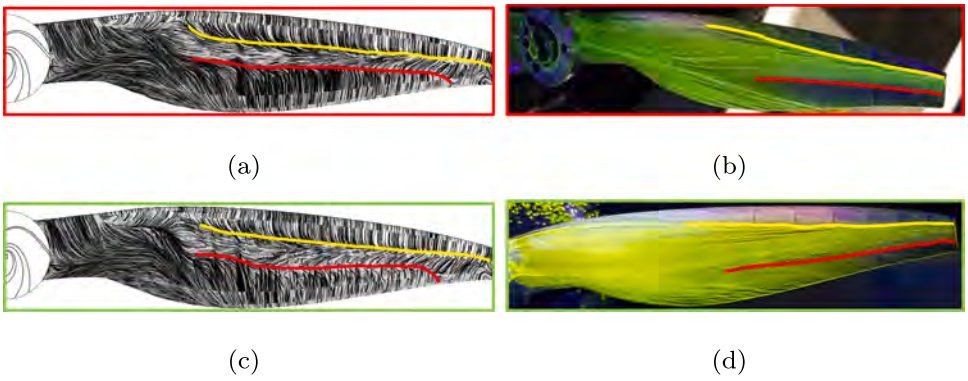


**Fig. 5.** Time-averaged surface streamlines and oil flow under (a-b) turbulent and (c-d) clean inflow. Yellow and red lines indicate separation and transition, respectively. For interpretation of the references to colour in this figure legend, the reader is referred to the web version of this article.

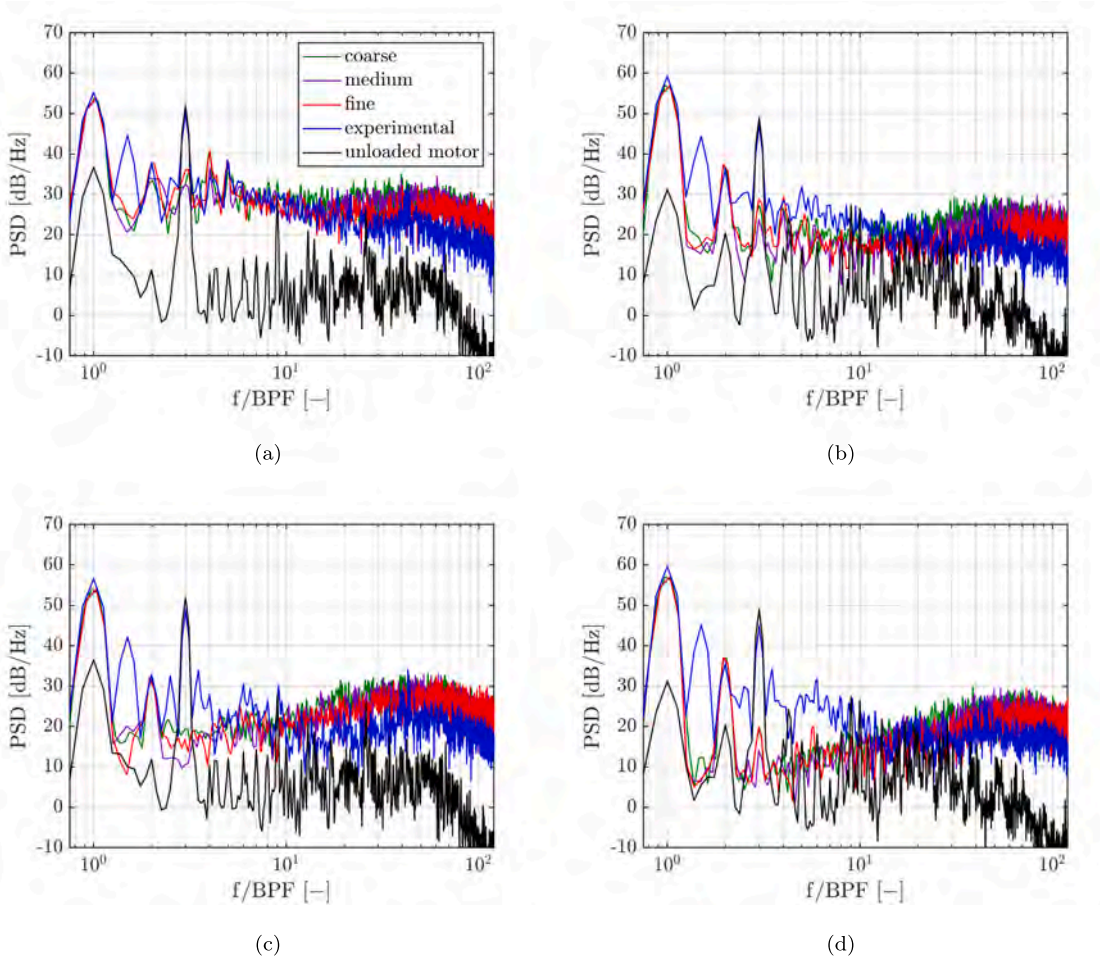


**Fig. 6.** Acoustic spectra for the propeller under (a-b) turbulent and (c-d) clean inflow conditions for (a,c) Mic.1 and (b,d) Mic.4.

the grid-generated turbulence is convected into the propeller, while the shear layer between the jet and the quiescent flow remains outside the propeller disk and does not interact with the blades. Downstream of the propeller disk, in both cases, the wake and tip vortices are clearly visible and remain well separated from the propeller plane. These observations indicate that, under the present operating conditions, no Blade–Wake Interaction (BWI) noise is generated.

Examining the mean flow, it is found that it exhibits a certain degree of inhomogeneity because of the propeller's proximity to the turbulence grid. It will be shown later that this has an impact on the far-field noise. To the authors' knowledge, this is not always checked in experiments, which mostly rely on single-point measurements for turbulence characterization. Fig. 8 shows the mean inflow distribution on a circular plane located at $x/R = -0.5$ upstream of the propeller, with and without the grid. In the presence of the grid (Fig. 8a), the inflow presents a regular pattern, which is expected to introduce peaks at the higher BPF harmonics in the unsteady loading spectrum. In particular, an almost square region of higher velocity is present (Fig. 8a), whose diagonal spans the rotor diameter, with local velocities ranging between 10.5 and 11 $\mathrm{m\,s^{-1}}$. Within this region, four distinct high-velocity spots can be identified,

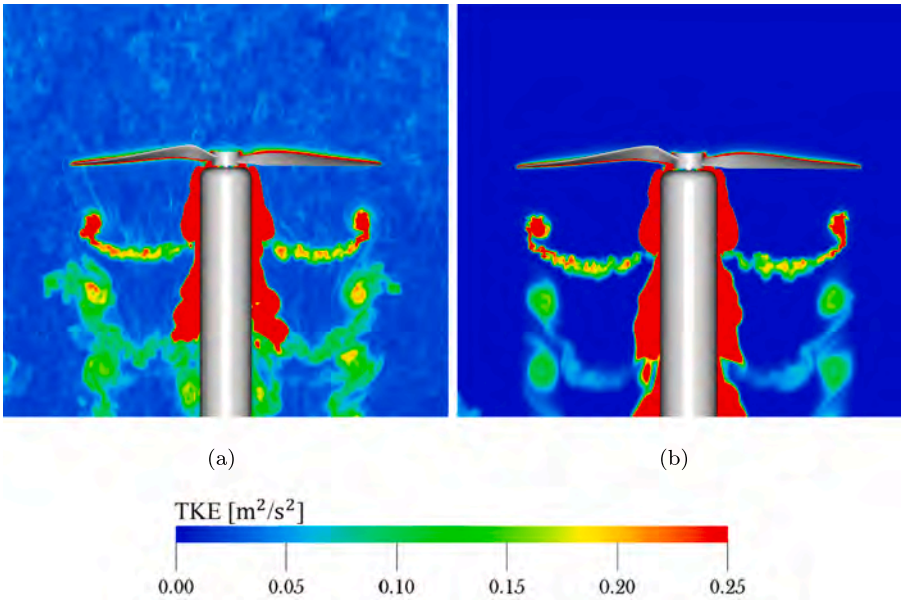


**Fig. 7.** Instantaneous snapshot of the Turbulent Kinetic Energy (TKE) field at the mid plane of the propeller for (a) turbulent and (b) clean case.

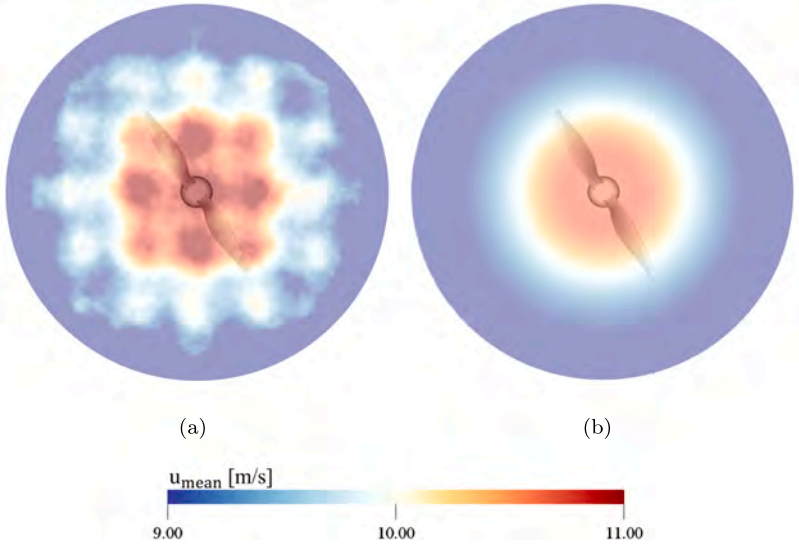


**Fig. 8.** Mean streamwise velocity $u_{\text{mean}}$ at $x/R = -0.5$ upstream of the propeller plane (a) with and (b) without the grid.

regularly distributed along the blade path. Therefore, it is expected that this inflow non-uniformity can induce a periodic component at the 2nd BPF harmonic in the unsteady blade loading. At the blade tip, the inflow velocity ranges from 10 to 10.5 m s$^{-1}$. Over one full revolution, the blade tip crosses eight alternating high- and low-velocity regions, suggesting that this inhomogeneity may also introduce a periodicity at the 4th BPF harmonic in the unsteady loading.

What qualitatively described above is confirmed in Fig. 9, where the phase-averaged unsteady sectional thrust is plotted over one revolution. The phase angle, $\phi$, varies from 0° to 360°. The trends are presented for three radial positions: $r/R = 0.5, 0.75$, and 1. Due to the limited number of revolutions sampled and the relatively high turbulence intensity, a clean phase-averaged signal cannot be obtained. However, the figure clearly shows that the dominant frequency of the loading fluctuations varies along the radius, shifting from the 2nd to the 4th BPF harmonic, as expected based on Fig. 8. This indicates that, in this configuration, the observed variations in the mean axial inflow can modulate the angle of attack, leading to periodic variations in the unsteady loading.

An inhomogeneous inflow introduces acoustic tones at higher BPF harmonics in the acoustic spectrum [56]. This occurs because the periodic blade loading, induced by the inflow inhomogeneity, introduces an additional periodicity into the acoustic signature, which is subsequently modulated by the BPF. In other words, the additional periodicity is carried by the fundamental frequency. This modulation implies that the Fourier representation of the acoustic signal necessarily contains a series of higher harmonics (both odd and even) of the fundamental frequency to accurately reconstruct the modulated waveform [57]. Therefore, the presence of tones at higher BPF harmonics is expected whenever such an inflow inhomogeneity exists, regardless of the specific periodicity of the inflow itself.

### 3.2. *Characterization of incoming turbulence in the absolute frame of reference*

The objective of this section is to obtain representative values of integral length scales and turbulence intensity to characterize the turbulent

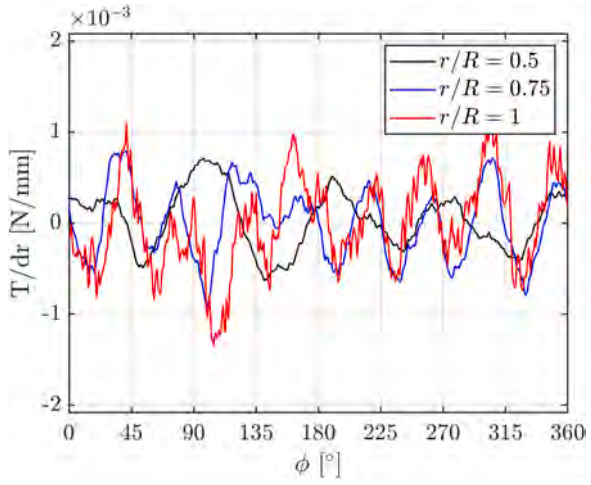


**Fig. 9.** Phase-averaged unsteady sectional thrust across one revolution at different radial positions.

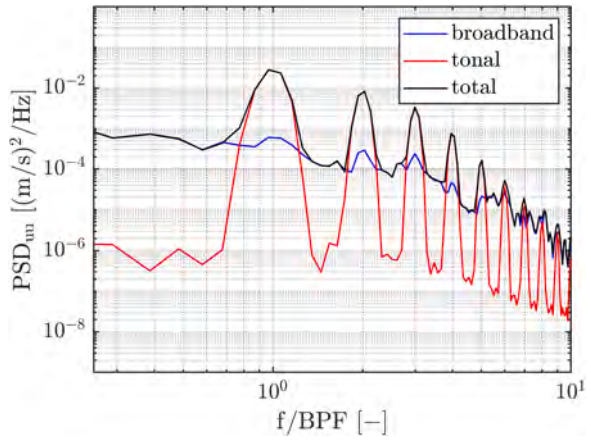


**Fig. 10.** Turbulence spectrum at $x/R = -0.2$ and $y/R = 0.5$ split into broadband and tonal components.

inflow. These parameters are typically used as input to Amiet's model. The analysis was performed in a plane perpendicular to the propeller plane.

Turbulence characterization in the presence of the propeller requires separating the tonal ($u'_{\text{tonal}}$) and broadband ($u'_{\text{broadband}}$) contributions. In particular, to properly compare the turbulent length scales and turbulence intensity of the incoming flow with and without the propeller, it is required to remove the peaks introduced by the blade passage. This is achieved by subtracting the phase-locked average from the instantaneous signal, thereby removing the periodic blade-passage component and isolating the broadband fluctuations [17,53]. The signal is first divided into $N$ cycles of the fundamental frequency. The ensemble average of these cycles yields the tonal component $u'_{\text{tonal}}$, which is then subtracted from the original signal $u'(x,t)$ to obtain the broadband component (Fig. 10). In this work, data are sampled over 10 revolutions, corresponding to 20 blade passages and thus 20 cycles of the fundamental frequency.

Fig. 11 compares the Power Spectral Densities (PSDs) of the broadband part of the streamwise velocity component with and without the propeller. The most noticeable differences occur at low frequencies, associated with the fluctuation of large coherent structures. These structures are strongly affected by the velocity gradients induced by the propeller, as their size makes them more sensitive to the spatial variations in the mean flow. At higher frequencies, related to smaller vortical structures, the spectra show smaller differences, indicating that small-scale turbulence is only weakly influenced by the propeller-induced gradients.

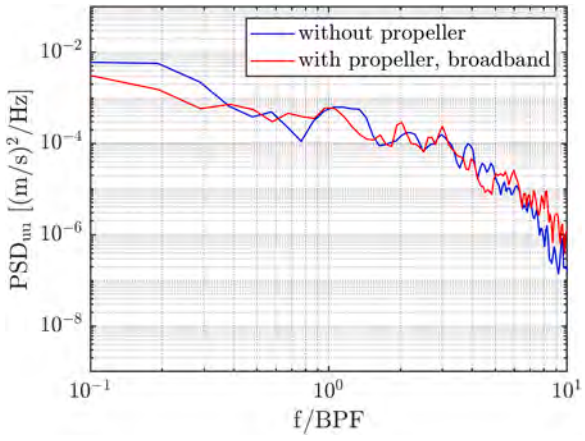


**Fig. 11.** Comparison between the spectra with and without the propeller at $x/R = -0.2$ and $y/R = 0.5$.

The following analysis focuses on the integral length scales and the root-mean-square (rms) of the streamwise fluctuations, since these are the dominant drivers of loading fluctuations. Once the broadband component is obtained, $u_{\text{rms}}(x)$ and $\Lambda_{uu,x}(x)$ are computed as follows:

$$u_{\text{rms}}(x) = \sqrt{\frac{\sum_{i=1}^{N}\left(u(x,t_i) - u_{\text{mean}}(x)\right)^2}{N}}, \tag{11}$$

$$\Lambda_{ij,m}(\mathbf{x}) = \int_0^\infty \rho_{ij,m}(\mathbf{x})\,\mathrm{d}l = \int_0^\infty \frac{\overline{u_i(\mathbf{x},t)u_j(\mathbf{x}+\mathbf{le_m},t)}}{u_{i,\text{rms}}(\mathbf{x})u_{j,\text{rms}}(\mathbf{x}+\mathbf{le_m})}\,\mathrm{d}l. \tag{12}$$

Here, $\rho_{ij,m}(\mathbf{x},l)$ denotes the normalized two-point correlation function, while $e_m$ indicates the direction along which the correlation is evaluated. The spatial autocorrelation is calculated on a segment of size $\Delta x = 0.5R$, and the data are time-averaged over the last 5 revolutions, since convergence is reached. Following the procedure of [58] and [53], the integral in Eq. (12) is evaluated up to the first zero crossing, and the resulting integral length scale is then assigned to the midpoint of the segment. The length of the segment is chosen as a compromise between two competing requirements: ensuring that the results are independent of the segment length, and positioning the segment as close as possible to the propeller plane. This trade-off is necessary because the plane used to evaluate $\Lambda_{uu,x}$ is constrained by the local reference frame encompassing the propeller. With this configuration, the closest point to the propeller plane, where $\Lambda_{uu,x}$ can be reliably evaluated, is at $x/R = -0.4$. The quantities are then averaged in the radial direction to obtain representative values of the characteristics turbulent inflow [53].

Figs. 12a and 12c present the streamwise evolution of the radially averaged root-mean-square of the streamwise fluctuations, $u_{\text{rms}}(x)$, together with the integral length scales, $\Lambda_{uu,x}(x)$ and $\Lambda_{uu,y}(x)$, for both cases with and without the propeller. As a reference, the results are compared with empirical scaling laws for naturally decaying turbulence [49,59]. The turbulence intensity reads

$$\text{TI}_u(x) = C\left(\frac{x}{d}\right)^{-\frac{5}{7}}, \tag{13}$$

while the integral length scales are

$$\frac{\Lambda_{uu,x}}{d} = I\sqrt{\frac{x}{d}}, \qquad \frac{\Lambda_{uu,y}}{d} = \frac{IJ}{2}\sqrt{\frac{x}{d}}. \tag{14}$$

Here, $x$ represents the distance from the grid, $d = 0.01\,\text{m}$ is a characteristic length of the grid (Fig. 3), and $C$, $I$ and $J$ are constants whose values are $C = 1.13$, $I = 0.2$ and $J = 1$ [49]. The disagreement between the results without the propeller and the empirical laws might be due

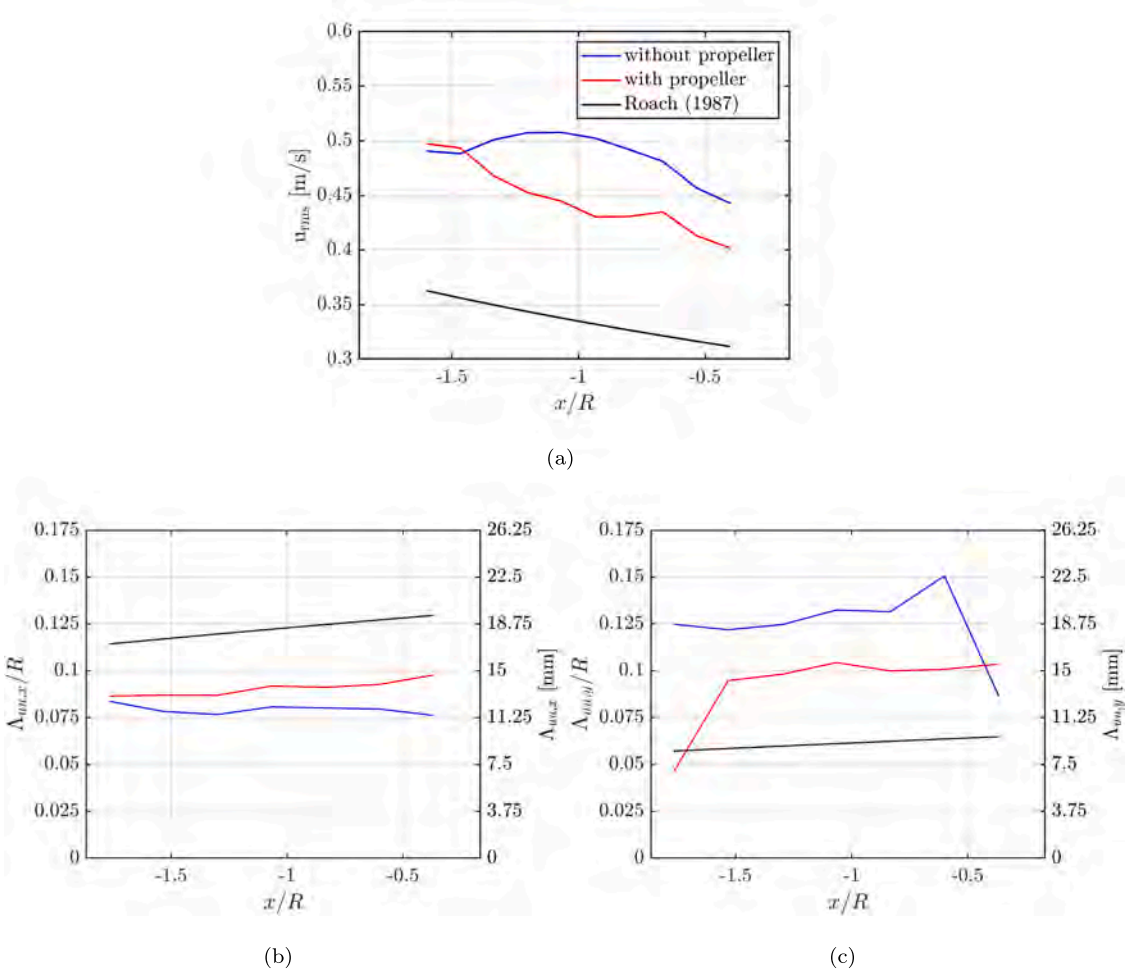


**Fig. 12.** Effects of propeller on the (a) rms and (b) longitudinal and (c) transverse integral length scales of the incoming turbulence. Data are radially averaged.

to the inhomogeneity of the turbulent flow. In fact, a minimum distance of 10 mesh sizes $M$ is required to completely homogenize the turbulence [49]. As a matter of fact, the relations in [49] are obtained over distances from the turbulence grid higher than $10\,M$, while, in the present study, the propeller is placed at $10\,M$ downstream of the grid.

Regarding $u_{\mathrm{rms}}$, its amplitude decreases when the propeller is installed (Fig. 12a). This small reduction is due to the weak streamtube contraction induced by the propeller: an elongation of the eddies in the $x$ direction reduces the amplitude of the fluctuation of the axial velocity component and increases the fluctuations of the other two velocity components [60,61].

The impact of the presence of the propeller on the integral length scales is shown in Figs. 12b and 12c. It can be observed that $\Lambda_{uu,y} \approx \Lambda_{uu,x}$ in the presence of the propeller, whereas $\Lambda_{uu,y} \approx 2\Lambda_{uu,x}$ without the propeller. This means that turbulence is not yet isotropic, since $\Lambda_{uu,y} = \Lambda_{uu,x}/2$ for isotropic turbulence. Besides, Fig. 12b shows that $\Lambda_{uu,x}(x)$ is generally higher in the case with the propeller. The increase in $\Lambda_{uu,x}$ is slightly steeper close to the propeller plane, in particular, where it grows to $0.1\,R$. Without the propeller, $\Lambda_{uu,x}$ is almost constant, with a value around $0.075\,R$. It is worth observing that, given the convective velocity $\mathrm{U_{conv}} \approx 10\,\mathrm{m\,s^{-1}}$, the radially averaged value is not large enough to satisfy the condition:

$$\frac{\Lambda_{uu,x}}{U_{\mathrm{conv}}} >> \frac{1}{\mathrm{BPF}}, \tag{15}$$

which ensures the blade-to-blade correlation and therefore the haystacking [15]. Indeed, a minimum value of $\Lambda_{uu,x} \approx 50\,\mathrm{mm}$ would be necessary to satisfy this condition. Therefore, no strong quasi-tonal noise due to this phenomenon is expected in the acoustic spectrum.

### 3.3. Characterization of incoming turbulence in the reference frame of the propeller

Turbulence interaction with the propeller is now investigated in the rotating reference frame, hence on a plane moving with the blade. Therefore, a comparison can be made with what happens when turbulence interacts with the leading edge of a wing in rectilinear motion. This analysis was performed on multiple planes at different radial positions $r$, but, for the sake of conciseness, only the results at $r/R = 0.6$ are presented here. No significant differences were observed at the other radial positions. In the next, $x$ and $y$ denote the streamwise and normal directions in the plane.

The distortion of turbulence resulting from interaction with the leading edge of an airfoil is governed by two distinct mechanisms. Their relative importance depends on the ratio between the eddy size, $l$, and a characteristic geometrical length of the airfoil, $a$ [36,40]. When the size of the incoming turbulent structure $l$ is much larger than the characteristic length of the airfoil $a$ ($l/a \gg 1$), the prevailing distortion mechanism is caused by the blockage exerted by the presence of the body. This causes the streamwise velocity fluctuations to reduce and the upwash one to increase because of the momentum transfer [36,52]. In contrast, when the size of the incoming turbulent structure $l$ is much smaller than the characteristic length of the airfoil ($l/a \ll 1$), the eddies are mainly deformed due to the distortion of the vorticity field. This mechanism induces a stretch of the eddy in the upwash direction, which reduces

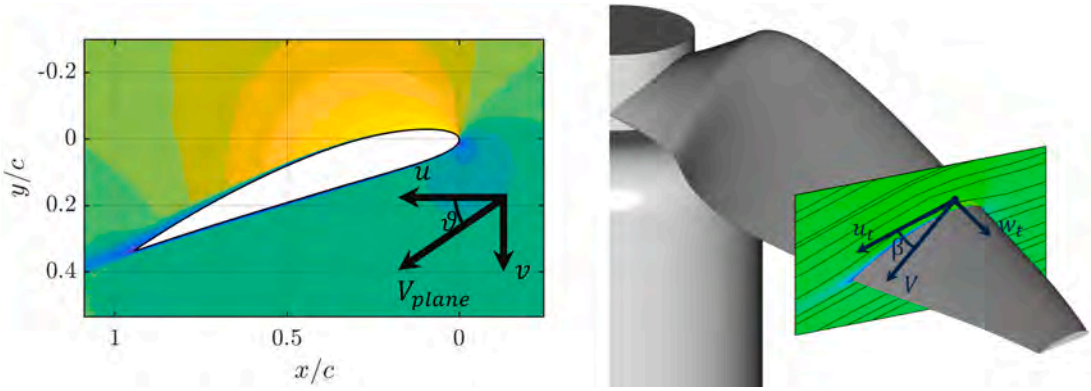


(a) (b)

**Fig. 13.** Local reference frame: $\vartheta$ identifies the planar local direction (Fig. 13a), while $u_t$ and $v_t$ (not represented in the sketch) are the tangent and normal planar components, $w_t$ is the out-of-plane component and $\beta$ is the angle between the velocity vector $V$ and $u_t$ (Fig. 13b).

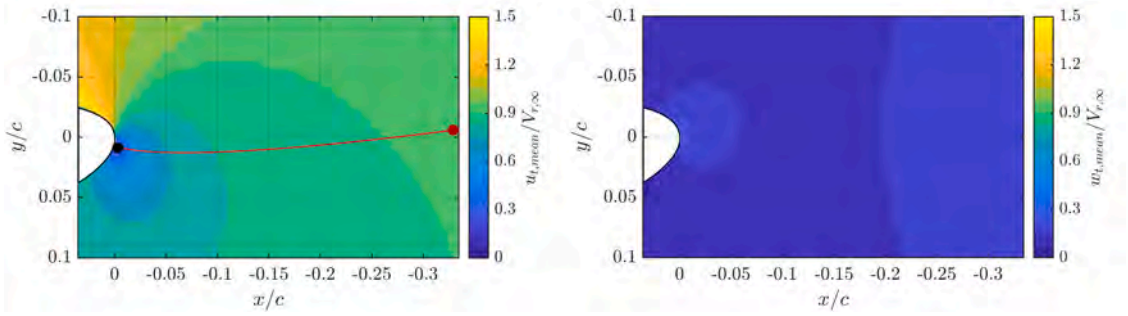


(a) (b)

**Fig. 14.** $u_{t,\mathrm{mean}}$ and $w_{t,\mathrm{mean}}$ close to the leading edge at $r/R = 0.6$. The red line in Fig. 14a individuates the local stagnation line. The spectrum of the upwash velocity $v_t$ shown in Fig. 16 is computed at the red and black points. For interpretation of the references to colour in this figure legend, the reader is referred to the web version of this article.

the fluctuations of the upwash velocity component [35,36]. It is worth noticing that, for the present case, due to the small thickness of the blade, in the present study, the fine mesh does not resolve structures smaller than the characteristic size of the blade.

Fig. 13 illustrates the local reference frame. $u$ and $v$ are the streamwise and normal components in the plane, whereas $w$ is the out-of-plane component. In Fig. 13a, $\vartheta$ identifies the direction of the local streamline with respect to the rotor plane. In Fig. 13b, the in-plane components $u$ and $v$ are projected onto the mean local streamline, resulting in the tangential and normal components, $u_t$ and $v_t$, respectively, relative to that streamline:

$$u_t = u\cos\vartheta + v\sin\vartheta; \tag{16}$$

$$v_t = u\sin\vartheta - v\cos\vartheta. \tag{17}$$

In the following, the mean value and the rms of the velocity components are normalized by the local upstream velocity $V_{r,\infty}$:

$$V_{r,\infty} = \sqrt{V_\infty^2 + (\omega r)^2}, \tag{18}$$

where $V_\infty$ is the absolute free-stream velocity, $\omega$ is the rotational speed, and $r$ is the local radius. Fig. 14a shows the contour of $u_{t,\mathrm{mean}}$ and the local stagnation line in a region near the leading edge. Following the local streamline, $u_{t,\mathrm{mean}}$ decelerates approaching the stagnation point as a consequence of the blockage due to the leading edge, while the mean normal component $v_{t,\mathrm{mean}}$ is zero everywhere and is not reported here. The out-of-plane component $w_{t,\mathrm{mean}}$ (Fig. 14b) slightly increases in front of the leading edge because of the three-dimensionality of the flow.

Fig. 15 shows the rms fields of the three velocity components near the leading edge. The amplitude of the fluctuations of the normal component $v_{t,\mathrm{rms}}$ (Fig. 15b) reaches a maximum approaching the stagnation point, whereas the streamwise component $u_{t,\mathrm{rms}}$ is damped (Fig. 15a). In contrast, the amplitude of the fluctuations of the normal component is enhanced as the streamwise velocity component decelerates close to the stagnation region. The out-of-plane component $w_t$ is weakly involved in this mechanism. These observations suggest a momentum transfer from the streamwise velocity component $u_t$ to the normal velocity component $v_t$, following the physical mechanism observed for the rectilinear motion [40,62].

Fig. 16a shows the PSD of the upwash velocity $v_t$ at $r/R = 0.6$ at the red and black points shown in Fig. 14. The spectrum of $v_t$ at corresponding points at $r/R = 0.7$ and $r/R = 0.9$ is also reported in Fig. 16b and Fig. 16c. Different from the rms contour plots above, where no major difference is visible between two radial stations, here another radial location is shown because some differences are more evident.

Across the whole range of frequencies solved with the current mesh, there is an overall increase in the energy level as the leading edge of the blade is approached. This is indeed an effect of the momentum transfer characterizing the distortion mechanism prevailing in the case of very large structures [36]. Since the points where the spectrum is computed are static with respect to the blade, the spectrum is predominantly broadband, and the strong potential effects due to the blade passage are not observed at the BPF harmonics. However, it is worth noticing the presence of small peaks around the 2$^{\mathrm{nd}}$ and 4$^{\mathrm{th}}$ harmonics in Fig. 16a and a higher peak at the 4$^{\mathrm{th}}$ harmonic in Figs. 16b and 16c. The origin of these peaks can be attributed to the non-homogeneity of the inflow described before. Indeed, a tonal component in a PSD performed in a rotating frame of reference indicates the presence of a spatial

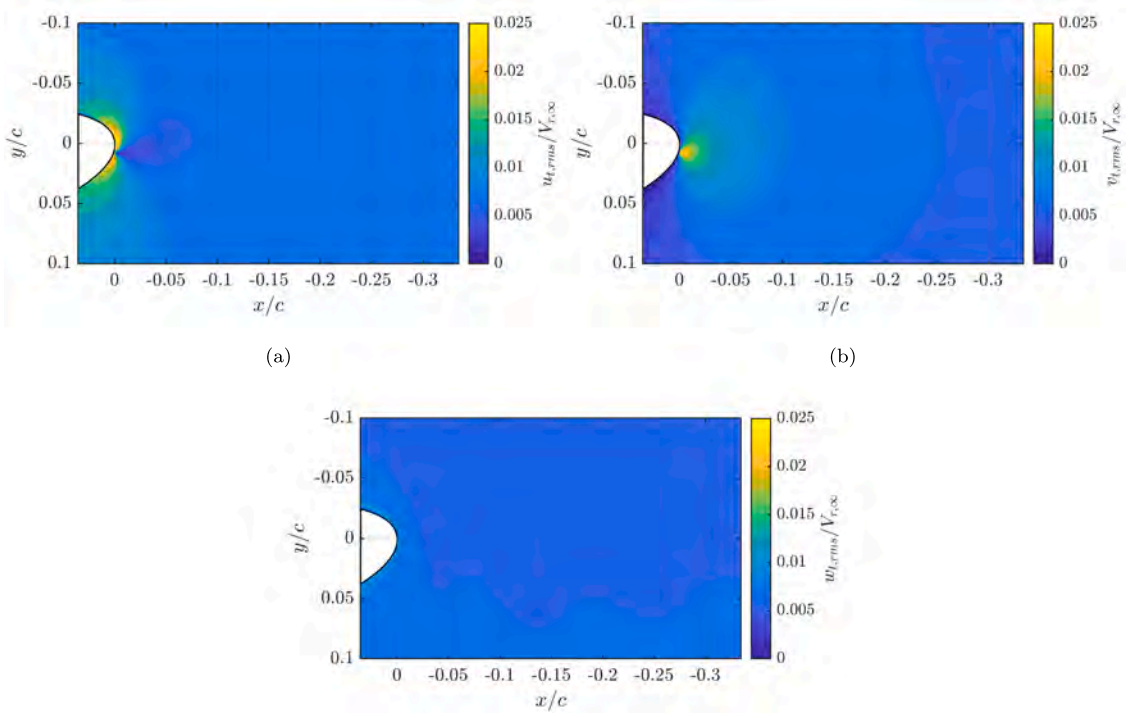


**Fig. 15.** Rms fields of the three velocity components close to the leading edge at $r/R = 0.6$.

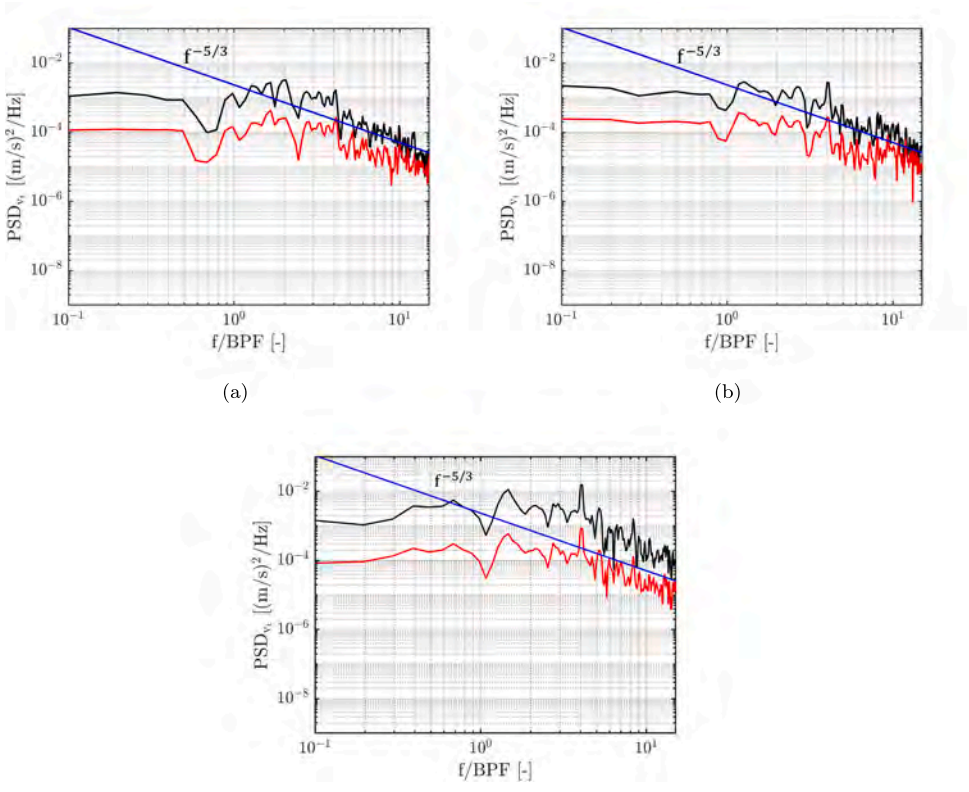


**Fig. 16.** PSD of the upwash velocity $v_t$ computed (a) at the red and black points shown in Fig. 14 at $r/R = 0.6$ and at corresponding points along the stagnation line at (b) $r/R = 0.7$ and (c) $r/R = 0.9$. Line colors refer to the sampling points in Fig. 14. For interpretation of the references to colour in this figure legend, the reader is referred to the web version of this article.

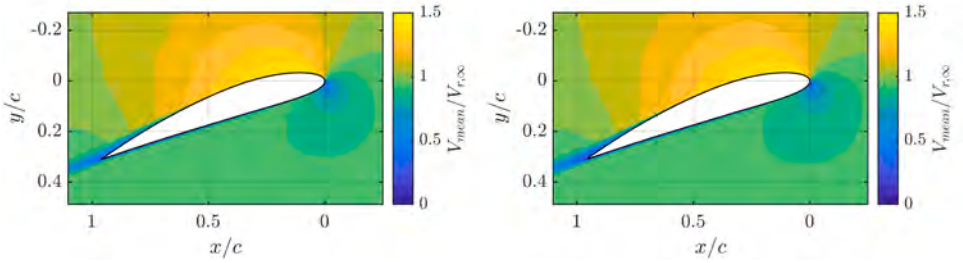


**Fig. 17.** Mean velocity field at $r/R = 0.6$ under (a) turbulent and (b) clean inflow conditions.

**Table 3**
Effect of ingested turbulence on time-averaged $C_T$ and $C_Q$.

| | Turbulent | Clean |
|---|---|---|
| $C_T$ | 0.0938 | 0.0947 |
| $C_Q$ | 0.0084 | 0.0084 |

periodicity, which corresponds to what is observed in Fig. 8. Moving toward the tip radius, the bump around the 2nd harmonic disappears, while the peak at the 4th harmonic becomes more pronounced, consistent with the observations on the inhomogeneity of the inflow in Section 3.1. It is interesting to observe that the intensity of these tones increases toward the leading edge along the stagnation line. This suggests that leading-edge distortion amplifies the effects of inhomogeneity in the inflow.

The analysis in this section suggests that the leading-edge-induced distortion qualitatively follows the physics of the 2D cases present in the literature. In particular, an increase in the intensity of the normal velocity fluctuations is observed. In addition, the spectrum of the upwash velocity exhibits tonal features around the higher harmonics of the BPF, due to the inflow inhomogeneity discussed in Section 3. Interestingly, the distortion induced by the leading edge further enhances these spectral peaks, thereby amplifying the effects of inflow non-homogeneity.

### 3.4. Impact of inflow turbulence on the flow over the blade

This section describes the impact of upstream turbulence on the flow over the blade and on the unsteady loading of the propeller. Fig. 17 shows the time-averaged velocity magnitude field normalized by the local free-stream velocity for the turbulent and clean inflow conditions. For the sake of conciseness, only the results at $r/R = 0.6$ are reported. No substantial difference is observed between the two cases. This is confirmed in Table 3, where the time-averaged thrust and torque coefficients are presented. Incoming turbulence causes a slight decrease (less than 1%) in the thrust coefficient $C_T$, while the torque coefficient $C_Q$ remains essentially unchanged.

To investigate the effect of upstream turbulence on the LSB, Fig. 18 presents the time-averaged streamlines on the suction side of the blade, superimposed on the mean pressure coefficient $c_p$, both for turbulent and clean cases. Here, $c_p$ is obtained by normalizing the surface pressure by the dynamic pressure at the tip. No significant differences are observed in the size and position of the LSB, if not that the flow reattaches slightly downstream in the clean case. This justifies the small reduction in the time-averaged $C_T$ in the turbulent case shown in Table 3. Since at the same Reynolds number the local angle of attack governs the mean properties of the LSB [16], the similar mean flow shown in Fig. 17 implies that the LSB behaves similarly in both cases.

More evident effects of the upstream turbulence on the LSB can be observed in Fig. 19, where the contours of the $c_{p,\mathrm{rms}}$ are reported for both turbulent and clean inflows. The incoming turbulent inflow causes an increase in the rms of the pressure fluctuations at the leading edge, along the separation line, and increases the amplitude of pressure fluctuations at the location of the LSB.

Fig. 20 shows the behavior of the mean $c_p$ (continuous line) and $c_{p,\mathrm{rms}}$ (shaded area) at 60% and 70% of $R$. Two radial sections are shown to strengthen the conclusions. The non-dimensional quantities are obtained by normalizing them with the local free-stream velocity defined in Eq. (18). The mean $c_p$ curves for the two inflow conditions are very similar, in agreement with the fact that, in this configuration, the steady loading is not significantly affected by upstream turbulence. The turbulent inflow introduces pressure fluctuations on the suction side upstream and across the LSB, which are obviously not present for the clean inflow up to the reattachment point. Under a turbulent inflow, after $c_{p,\mathrm{rms}}$ peak, the amplitude of the pressure fluctuations experiences an initial attenuation, followed by an increase in their amplitude at the location of the LSB. The differences in $c_{p,\mathrm{rms}}$ between the clean and turbulent inflow cases vanish after the reattachment point, from where a turbulent boundary layer develops toward the trailing edge. Conversely, on the pressure side, the amplitude of the fluctuations tends to decrease toward the trailing edge. The behavior is similar for the two radial positions.

To highlight the differences in unsteady surface pressure across frequencies, Fig. 21 presents the deviation between the PSDs of surface pressure under turbulent and clean inflow conditions, evaluated along the chord at 60% and 70% of the tip radius $R$. On the suction side (Figs. 21a and 21b), at frequencies lower than the 10th BPF harmonic, the largest deviation is observed at the leading edge, where the turbulent inflow impinges. Moving towards the trailing edge, the difference over this range of frequencies is reduced. In the region upstream of the reattachment point, the maximum difference is found around the fourth BPF harmonic, because of the interaction with the inhomogeneous inflow shown in Fig. 8a. Other smaller bumps in the difference between the turbulent and clean cases are observed at harmonics and interharmonics of the BPF.

At frequencies between the 10th and 30th BPF harmonics, the increase in PSD observed in the turbulent inflow case decays more rapidly from the leading edge to the separation line compared to fluctuations at frequencies below the 10th BPF harmonic. A certain level of fluctuation intensity is present at the location of the LSB, particularly near the reattachment line. At frequencies higher than the 30th BPF harmonic, the greatest differences occur at the LSB location, where the amplitude of the fluctuations increases. After the reattachment point and across the entire frequency spectrum, the differences between the two inflow conditions reduce and tend to vanish as the turbulent boundary layer develops toward the trailing edge. These results confirm that the incoming turbulence increases the fluctuations where the LSB is. This behavior is highlighted in Figs. 21c and 21d, which show the delta in the surface pressure PSDs on the pressure side between the turbulent inflow and clean inflow cases. Since no LSB forms on the pressure side, the region of influence of upstream turbulence persists along the chord and extends downstream nearly to the trailing edge.

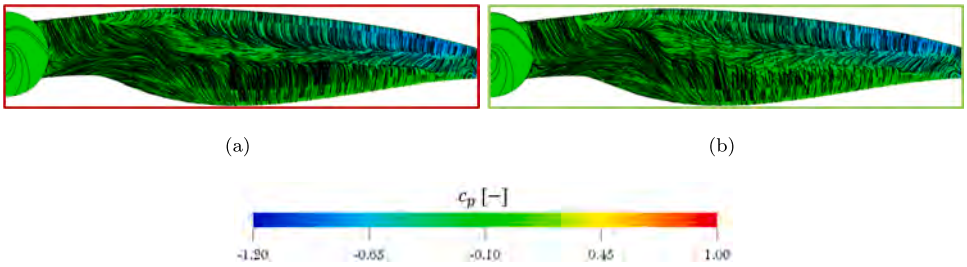


**Fig. 18.** Time-averaged $c_p$ and surface streamlines under (a) turbulent and (b) clean inflow conditions.

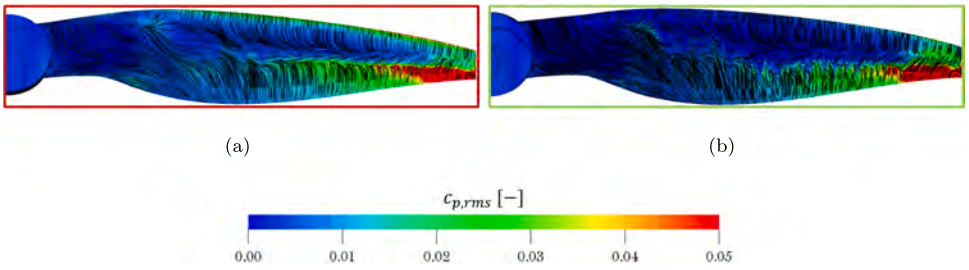


**Fig. 19.** $c_{p,\mathrm{rms}}$ and time-averaged surface streamlines under (a) turbulent and (b) clean inflow conditions.

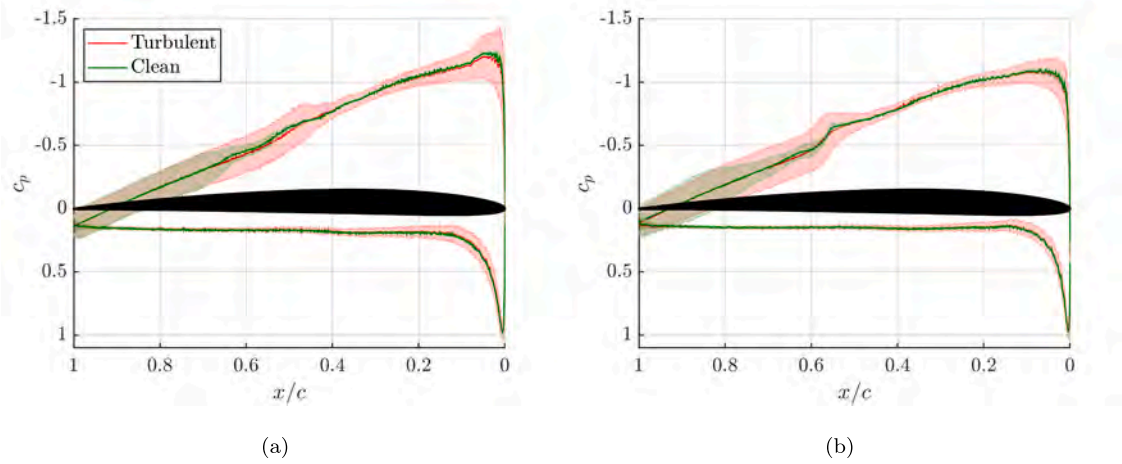


**Fig. 20.** $c_p$ at $r/R = 0.6$ (a) and 0.7 (b) under turbulent (▬) and clean (▬) inflow conditions. The width of the shaded region identifies the $c_{p,\mathrm{rms}}$.

### 3.5. Acoustic sources

Fig. 22 presents the directivity patterns for both turbulent and clean inflow conditions in terms of overall acoustic sound pressure level (OASPL) and three selected frequency bands. Under turbulent inflow, an increase in OASPL is observed, mainly along the propeller axis (Fig. 22a). The 1st BPF harmonic (Fig. 22b) is the same for both turbulent and clean inflow, except along the propeller axis, where the noise at the BPF vanishes for the clean case. In contrast, large differences are observed in the frequency range from the 3rd to the 20th BPF harmonics (Fig. 22c). Within this range, directivity exhibits a dipolar pattern for both inflow conditions but differences in sound pressure level up to 10 dB are visible almost in all directions. The high-frequency range instead (Fig. 22d) does not appear to be significantly affected by the turbulent inflow.

Going into more detail on the effects of turbulent inflow on the acoustic response, Figs 23a and 23b present the far-field noise spectra at Mics. 1 and 4, corresponding to the upstream direction and the propeller plane, respectively, for both turbulent and clean inflows. The turbulent-inflow case is expected to affect the far-field noise, particularly along the propeller axis, when compared with the clean inflow condition.

An increase in the broadband floor up to the 20th BPF harmonic is observed when turbulence is ingested. Furthermore, additional tones, not present for the clean-inflow case, can be noticed at harmonics higher than the 2nd one. Upstream turbulence does not appear to affect the first harmonic, as this is dominated steady loading and thickness noise. The effect on the 2nd BPF depends on the observer location. In the upstream direction (Mic. 1), a difference greater than 5 dB is observed between the turbulent and clean configurations, whereas no significant discrepancy is detected in the propeller plane (Mic. 4). For frequencies higher than the 20th BPF harmonic, where trailing-edge noise is dominant, the spectra collapse. Peaks at integer multiples of the BPF, associated with the previously described inflow non-homogeneity, are clearly visible. As stated in Section 3.1, the appearance of higher BPF harmonics in the acoustic spectrum, which are not observed in the loading spectrum, is associated with a modulation mechanism.

The contributions of the various aerodynamic noise sources to the far-field sound at a specific location are now identified using constructive and destructive power maps [16]. This analysis is performed using the FW-H solver Optydb-pfnoisescan. This methodology consists of applying the FW-H analogy to the surface-pressure fluctuations on both the entire surface and on each surface element $k$. These yield the total

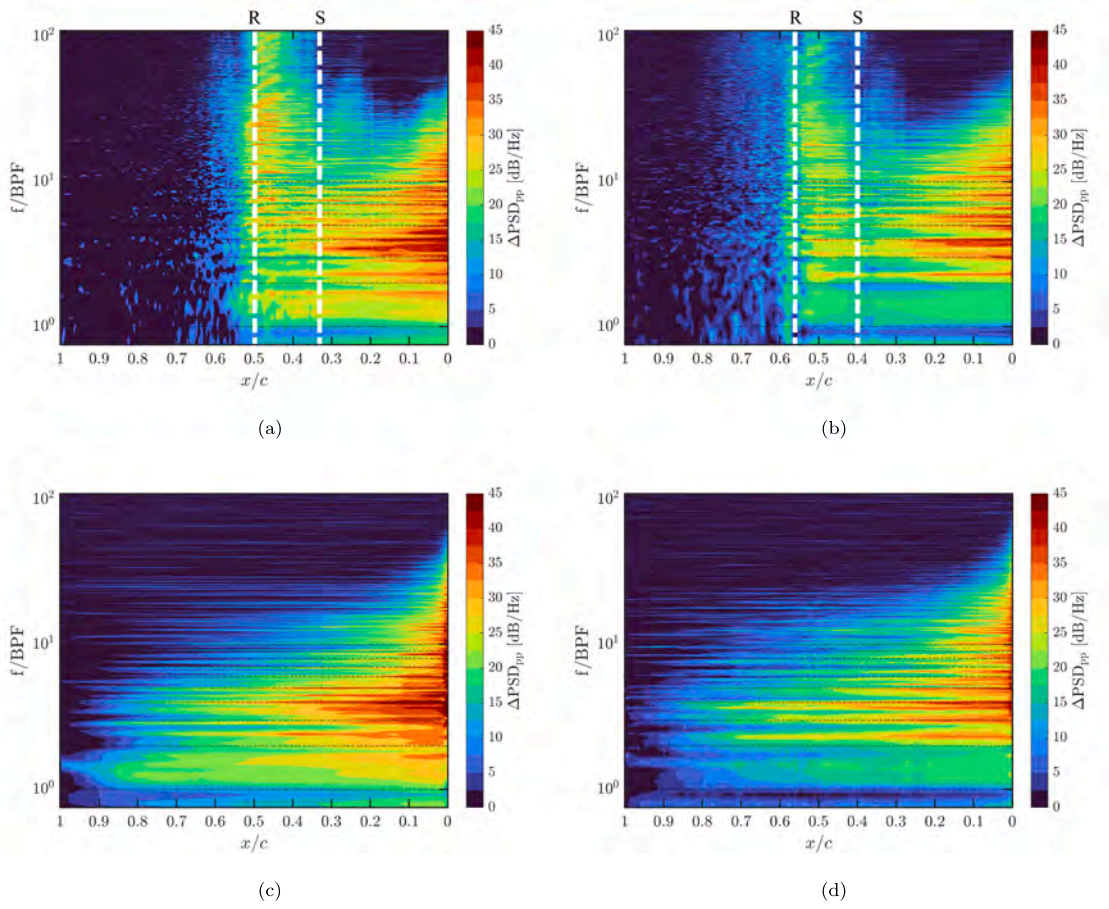


**Fig. 21.** ΔPSD of the surface pressure between turbulent and clean inflow conditions on the (a-b) suction and (c-d) pressure sides, at (a,c) $r/R = 0.6$ and (b,d) 0.7. The yellow and red vertical lines identify the separation and reattachment points, respectively. The white vertical lines indicate the separation (S) and reattachment (R) points, while the shaded horizontal dotted lines mark the harmonics from the 1st to the 10th. For interpretation of the references to colour in this figure legend, the reader is referred to the web version of this article.

acoustic pressure $p'_{\text{tot}}(t)$ and the acoustic pressure $p'_k(t)$ generated by element $k$, respectively. The cross-spectral coherence is then calculated by performing a Fourier Transform, indicated with $\hat{(\cdot)}$, as follows:

$$P_k(\text{f}) = \frac{\hat{p}^*_{tot}(\text{f})\hat{p}_k(\text{f})}{\Delta\text{f}|\hat{p}^*_{tot}(\text{f})|}. \tag{19}$$

The notation $(\cdot)^*$ is used to denote the complex conjugate. This cross-spectral density is then averaged over the frequency range with bandwidth Δf. The constructive (CP) and destructive (DP) powers are then obtained by taking the real part of $P_k(\text{f})s$, with $s = 1$ for CP and $s = -1$ for DP. Therefore, these two quantities are complementary. In other words, CP and DP are calculated from the coherence between the acoustic pressure radiated from the surface element and the total acoustic pressure at the same location [16], and indicate whether the element $k$ contributes constructively or destructively to $p'_{tot}(t)$.

Fig. 24 shows the CP and DP maps, expressed in dB, to the far-field noise at Mic. 1 over three frequency ranges, with a bandwidth Δf = 200 Hz and centered around the 1st, 3rd, and 50th harmonics of the BPF. For the band centered at the 1st BPF (100 Hz ≤ f ≤ 300 Hz, in Figs. 24a and 24d), the spectra collapse and the CP maps do not show any relevant difference. The constructive contribution comes mainly from the region close to the leading edge, while the LSB contributes destructively to the first tone. For the band centered at the 3rd harmonic (500 Hz ≤ f ≤ 700 Hz, in Figs. 24b and 24e), the difference in PSD between the clean and turbulent inflow is 20 dB Hz$^{-1}$. Under turbulent inflow conditions, the entire region that extends from the leading edge to the reattachment line contributes constructively to the noise over this frequency range. This confirms that the interaction between the turbulent inflow and the LSB contributes to tonal noise in the mid-frequency range. However, the tonal noise in this range originates at the leading edge and is due to the presence of tones in the inflow velocity spectrum, linked to the inhomogeneity of the inflow. For the band centered at the 50th harmonic (9.9 kHz ≤ f ≤ 10.1 kHz, in Figs. 24c and 24f), the CP and DP maps show a series of alternating constructive and destructive bands in the region from the leading edge to the LSB. These alternating bands reciprocally cancel out their contributions. The main contribution to acoustics in this frequency range is due to the turbulent boundary layer, characterized by a reduced correlation length, scattered at the trailing edge.

### 3.6. Identification and separation of turbulence and flow inhomogeneity effects using Amiet's model

In this section, data obtained in Section 3.2 are used as input to Amiet's model to confirm that the tonal peaks are due to the flow inhomogeneity rather than to the impingement of the turbulent inflow. The model requires a turbulence spectrum and predicts the component of the acoustic spectrum arising from the interaction of the propeller with the turbulent field. The reader may refer to the works of [30] and [32] for a comprehensive overview of the model, which is beyond the scope of the present work. The formulation of Amiet's model employed in this section is the one proposed by [34], which modifies the original formulation to allow a one-dimensional velocity spectrum (sampled or analytically modeled) to be used as input in the model. This is obtained by implementing a strip theory approach for the discretization of the blade in the radial direction [33] in its inverse formulation [63].

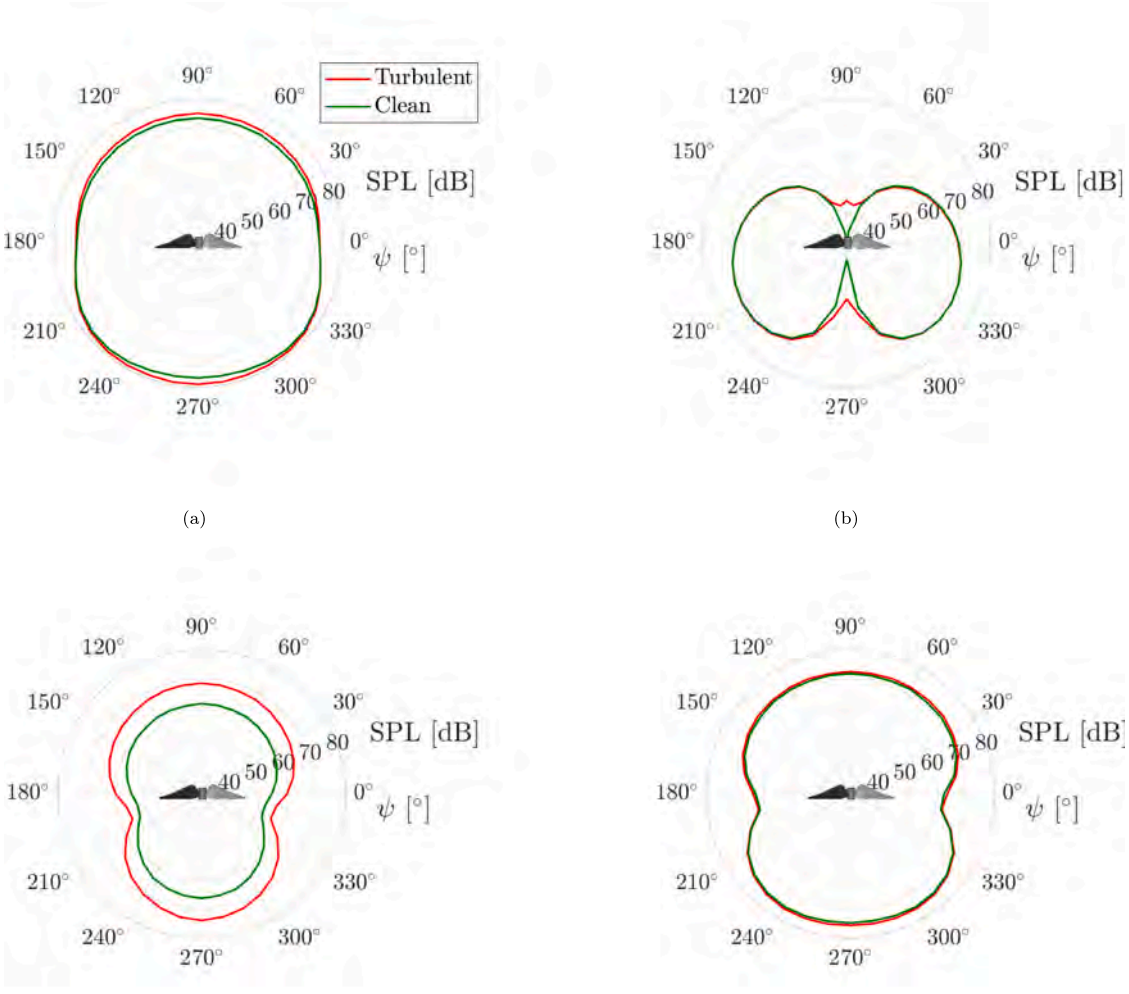


**Fig. 22.** Directivity plots for the (a) OASPL, (b) 1st BPF harmonic and the frequency ranges corresponding to (c) 3rd – 20th and (d) 30th – 100th BPF harmonics.

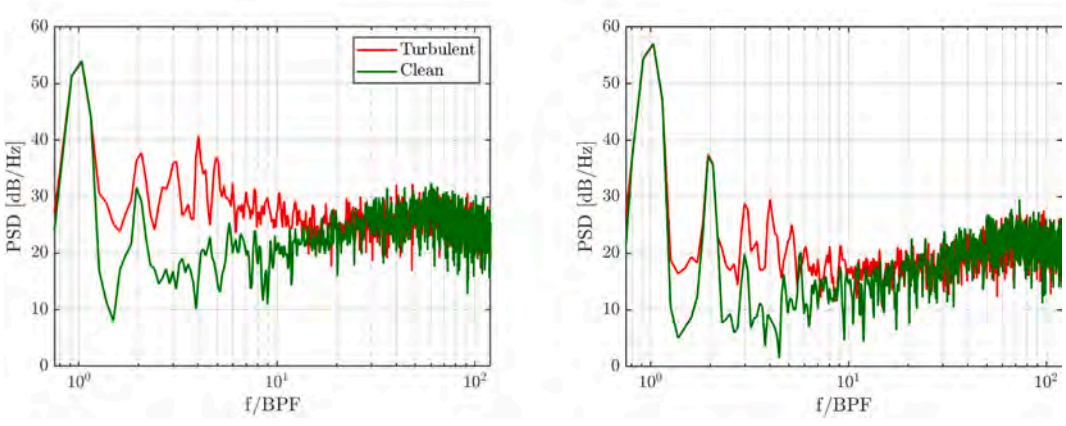


**Fig. 23.** Comparison between acoustic spectra under turbulent and clean inflows, at (a) Mics. 1 and (b) 4.

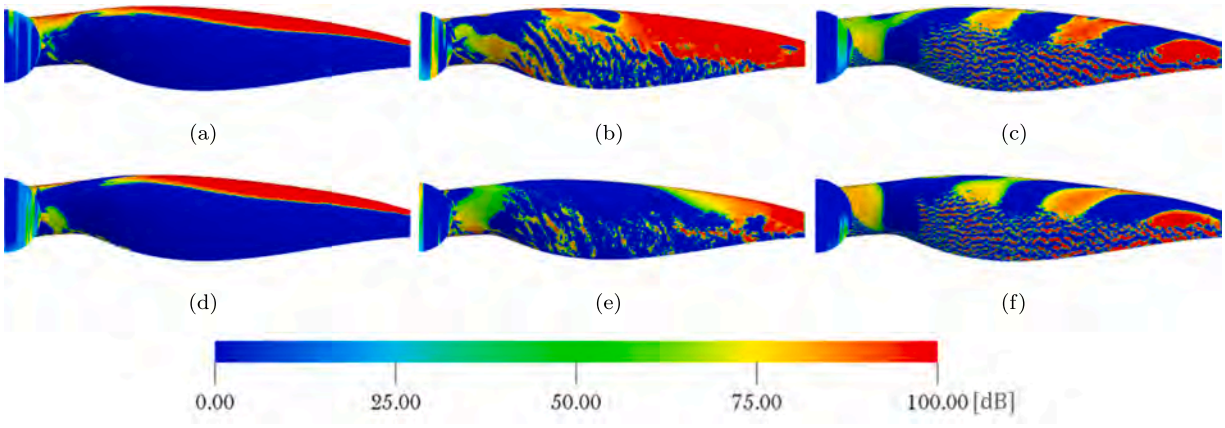


**Fig. 24.** CP maps at Mic. 1 under (a-c) turbulent and (d-f) clean inflow conditions over 100 Hz ≤ f ≤ 300 Hz (a,d), 500 Hz ≤ f ≤ 700 Hz (b,e), and 9.9 kHz ≤ f ≤ 10.1 kHz (c,f).

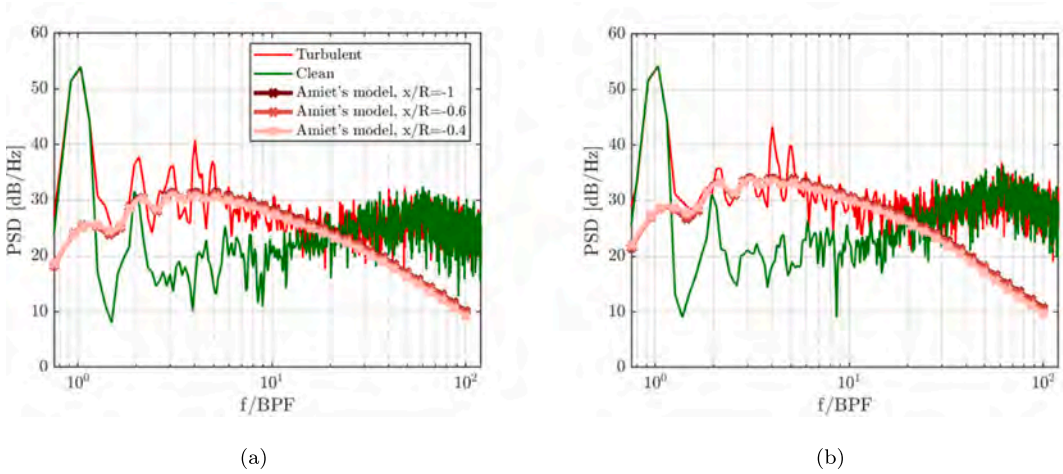


**Fig. 25.** Effect of turbulence distortion on the prediction of turbulence impingement noise with Amiet's model at (a) Mics. 1 and (b) 8.

Fig. 25 compares the acoustic spectra obtained using the FW–H analogy with those predicted by Amiet's model when varying the turbulence characteristics provided as input. In particular, the values of $\Lambda_{uu,x}$ and $u_{\mathrm{rms}}$, used to scale the analytical von Kármán velocity spectrum as input to the model, are taken at three upstream positions relative to the propeller plane. In the same plot, the acoustic spectrum for the clean case is included as a reference for the steady-loading noise. As shown in Table 3, the steady loading is not affected by the incoming turbulence, which is evident from the unchanged amplitude of the first harmonic between the two inflow cases. The effect of upstream turbulence at the first harmonic remains masked by the dominant steady loading and thickness noise.

It can be observed that the Amiet model's prediction, at this operating condition, varies slightly depending on the sampling location as expected from the characterization of the turbulent inflow. It is relevant to notice that Amiet's model provides a broadband increase in noise in the low-to-mid frequency range ($1^{\mathrm{st}}$BPF < f < $15^{\mathrm{th}}$BPF) similar to the one obtained from the FWH results. On the other hand, at higher frequencies (f > $20^{\mathrm{th}}$ – $30^{\mathrm{th}}$BPF), trailing-edge noise prevails.

It can be further observed that mid-frequency tones are present only in the turbulent case. As mentioned earlier, the values of $\Lambda_{uu,x}$ are too small to satisfy the condition in Eq. (15), which can cause quasi-tonal noise due to strong blade-to-blade correlation. Therefore, the comparison with Amiet's model confirms that tones, in the low-to-mid frequency range, are due to the unsteady loading caused by the mean flow inhomogeneity. This result highlights the importance of ensuring a highly uniform mean flow in simulations and experiments designed to characterize the effect of FST on propeller aeroacoustics, since inflow inhomogeneity affects the acoustic spectrum within the same frequency range as the ingested turbulence.

## 4. Conclusions

This paper investigates the interaction between a propeller operating at low Reynolds number and a grid-induced turbulent inflow. The goals are to characterize how the turbulent inflow changes when impinging on the propeller leading edge, how it affects the propeller aerodynamics, including the laminar separation bubble, and the aeroacoustics sources.

Three test cases are investigated: a turbulent jet, a case with the propeller in a uniform clean inflow, and a case with the propeller in the presence of turbulent inflow. The simulation setups replicate experiments carried out at TU Delft, which are also used as a reference for validating the numerical results.

It is found that the streamtube contraction, due to the presence of the rotor, elongates the largest eddies in the streamwise direction, reducing the intensity of the streamwise velocity fluctuations and the transversal integral length scale $\Lambda_{uu,y}$ with respect to the case of a free turbulent jet. Turbulence impinging on the rotor blades does not significantly affect the time-averaged flow field, the size and location of the laminar separation bubble, and the time-averaged thrust and torque coefficients. However, it is found, by looking at the rms of the surface pressure coefficient, $c_{p,\mathrm{rms}}$, that, for this case study, the presence of inflow turbulence increases the amplitude of the surface pressure fluctuations up to the laminar separation bubble reattachment point. Downstream of the

reattachment point, almost no difference is found between the turbulent and clean inflow cases. Therefore, the turbulent boundary layer downstream of the reattachment point develops similarly in the two cases.

The primary effect of the ingested turbulence on the far-field noise is to increase the broadband floor up to the $10^{th}$ BPF and to generate low-to-mid frequency tones. By performing noise source analysis on the blades' surface and using Amiet's model with data sampled upstream of the blade, it is demonstrated that these tones are caused by an inhomogeneity in the inflow, visible in the mean flow field, due to the presence of the grid. The flow inhomogeneity induces a periodic modulation in the inflow pattern to which the propeller is subject during a rotation. This is responsible for a periodic unsteady loading that causes the tonal peaks. These results underscore the necessity of maintaining uniform mean flow in simulations and experiments investigating the influence of free-stream turbulence on propeller aeroacoustics, as inflow inhomogeneities alter the acoustic spectrum over the same frequency range as the ingested turbulence.

## CRediT authorship contribution statement

**Mario Alì:** Writing – original draft, Visualization, Validation, Methodology, Investigation, Formal analysis, Data curation, Conceptualization; **Andrea Piccolo:** Writing – review & editing, Validation, Methodology, Conceptualization; **Riccardo Zamponi:** Writing – review & editing, Supervision, Conceptualization; **Daniele Ragni:** Writing – review & editing, Supervision, Conceptualization; **Francesco Avallone:** Writing – review & editing, Supervision, Software, Resources, Project administration, Funding acquisition, Conceptualization.

## Data availability

Data will be made available on request.

## Declaration of competing interest

The authors declare that they have no known competing financial interests or personal relationships that could have appeared to influence the work reported in this paper.

## Acknowledgements

The authors acknowledge Fondazione Compagnia di San Paolo for funding and supporting this project, and ISCRA for providing the computational resources. They also wish to thank Sara Montagner from Politecnico di Torino for sharing the experimental data used to validate the numerical setup.

## References

[1] S. Lee, S. Lee, Numerical and experimental study of aerodynamic noise by a small wind turbine, Renew. Energy 65 (2014) 108–112. https://doi.org/10.1016/j.renene.2013.07.036
[2] W.N. Alexander, W.J. Devenport, S.A.L. Glegg, Noise from a rotor ingesting a thick boundary layer and relation to measurements of ingested turbulence, J. Sound Vib. 409 (2017) 227–240. https://doi.org/10.1016/j.jsv.2017.07.056
[3] R.W. Paterson, R.K. Amiet, Noise of a model helicopter rotor due to ingestion of turbulence, Technical Report, 1979.
[4] Z. Xiong, W. Rui, L. Lu, G. Zhang, X. Huang, Experimental investigation of broadband thrust and loading noise from pumpjet due to turbulence ingestion, Ocean Eng. 255 (2022) 111408. https://doi.org/10.1016/j.oceaneng.2022.111408
[5] C. Doolan, D. Moreau, Flow Noise: Theory, Springer Nature, 2022.
[6] L. Kapustina, N. Izakova, E. Makovkina, M. Khmelkov, The global drone market: main development trends, in: SHS Web of Conferences, 129, EDP Sciences, 2021, p. 11004. https://doi.org/10.1051/shsconf/202112911004
[7] A. Gupta, T. Afrin, E. Scully, N. Yodo, Advances of UAVs toward future transportation: the state-of-the-art, challenges, and opportunities, Future Transp. 1 (2) (2021) 326–350. https://doi.org/10.3390/futuretransp1020019
[8] M.M. Connors, Factors that Influence Community's Acceptance of Noise: An Introduction for Urban Air Mobility, Technical Report, 2019.
[9] A. Plioutsias, N. Karanikas, M.M. Chatzimihailidou, Hazard analysis and safety requirements for small drone operations: to what extent do popular drones embed safety?, Risk Anal. 38 (3) (2018) 562–584. https://doi.org/10.1111/risa.12867
[10] C. Ramos-Romero, N. Green, S. Roberts, C. Clark, A.J. Torija, Requirements for drone operations to minimise community noise impact, Int. J. Environ. Res. Public Health 19 (15) (2022) 9299. https://doi.org/10.3390/ijerph19159299
[11] R. Frehlich, Y. Meillier, M.L. Jensen, B. Balsley, R. Sharman, Measurements of boundary layer profiles in an urban environment, J. Appl. Meteorol. Climatol. 45 (6) (2006) 821–837. https://doi.org/10.1175/JAM2368.1
[12] D. Casalino, G. Romani, R. Zhang, H. Chen, Lattice-Boltzmann calculations of rotor aeroacoustics in transitional boundary layer regime, Aerosp. Sci. Technol. 130 (2022) 107953. https://doi.org/10.1016/j.ast.2022.107953
[13] M. Sturm, T. Carolus, Tonal fan noise of an isolated axial fan rotor due to inhomogeneous coherent structures at the intake, Noise Control Eng. J. 60 (6) (2012) 699–706. https://doi.org/10.3397/1.3701041
[14] J.E. Ffowcs Williams, D.L. Hawkings, Sound generation by turbulence and surfaces in arbitrary motion, Philosophical Trans. Royal Society of London. Series A, Math. and Phys. Sci. 264 (1151) (1969) 321–342. https://doi.org/10.1098/rsta.1969.0031
[15] S. Glegg, W. Devenport, Aeroacoustics of low Mach number flows: fundamentals, analysis, and measurement, Academic Press, 2017.
[16] D. Casalino, G. Romani, L.M. Pii, R. Colombo, Flow confinement effects on sUAS rotor noise, Aerosp. Sci. Technol. 143 (2023) 108756. https://doi.org/10.1016/j.ast.2023.108756
[17] C.S. Thurman, N.S. Zawodny, N.A. Pettingill, The effect of boundary layer character on stochastic rotor blade vortex shedding noise, in: The Vertical Flight Society's 78Th Annual Forum and Technology Display, 2022.
[18] R. Hain, C.J. Kähler, R. Radespiel, Dynamics of laminar separation bubbles at low-Reynolds-number aerofoils, J. Fluid Mech. 630 (2009) 129–153. https://doi.org/10.1017/S0022112009006661
[19] M.M. O'meara, T.J. Mueller, Laminar separation bubble characteristics on an airfoil at low Reynolds numbers, AIAA J. 25 (8) (1987) 1033–1041. https://doi.org/10.2514/3.9739
[20] T.R. Ricciardi, W.R. Wolf, Switch of tonal noise generation mechanisms in airfoil transitional flows, Phys. Rev. Fluids 7 (8) (2022) 084701. https://doi.org/10.1103/PhysRevFluids.7.084701
[21] T. Jaroslawski, M. Forte, O. Vermeersch, J.-M. Moschetta, E.R. Gowree, Disturbance growth in a laminar separation bubble subjected to free-stream turbulence, J. Fluid Mech. 956 (2023) A33. https://doi.org/10.1017/jfm.2023.23
[22] E. Grande, G. Romani, D. Ragni, F. Avallone, D. Casalino, Aeroacoustic investigation of a propeller operating at low reynolds numbers, AIAA J. 60 (2) (2022) 860–871. https://doi.org/10.2514/1.J060611
[23] T. Jaroslawski, M. Forte, J.-M. Moschetta, E.R. Gowree, Boundary layer forcing on a rotating wing at low reynolds numbers, Exp. Fluids 64 (3) (2023) 58.
[24] E. Grande, D. Ragni, F. Avallone, D. Casalino, Laminar separation bubble noise on a propeller operating at low reynolds numbers, AIAA J. 60 (9) (2022) 5324–5335. https://doi.org/10.2514/1.J061691
[25] N.S. Jamaluddin, A. Celik, K. Baskaran, D. Rezgui, M. Azarpeyvand, Experimental analysis of a propeller noise in turbulent flow, Phys. Fluids 35 (7) (2023). https://doi.org/10.1063/5.0153326
[26] M. Sevik, Sound radiation from a subsonic rotor subjected to turbulence, Fluid Mech., Acoust., Design of Turbomachinery, Pt. 2 (1974).
[27] D.B. Hanson, Spectrum of rotor noise caused by atmospheric turbulence, J. Acoust. Soc. Am. 56 (1) (1974) 110–126. https://doi.org/10.1121/1.1903241
[28] W.K. Blake, Mechanics of flow-induced sound and vibration. volume 1 general concepts and elementary source. volume 2-Complex flow-structure interactions, Aplikace Matematiky, Appl. Math. 1 (1986).
[29] M.J. Hagen, G.K. Yamauchi, D.B. Signor, M. Mosher, Measurements of atmospheric turbulence effects on tail rotor acoustics, Technical Report, 1994.
[30] R.K. Amiet, Acoustic radiation from an airfoil in a turbulent stream, J. Sound Vib. 41 (4) (1975) 407–420. https://doi.org/10.1016/S0022-460X(75)80105-2
[31] R.K. Amiet, Noise produced by turbulent flow into a propeller or helicopter rotor, AIAA J. 15 (3) (1977) 307–308. https://doi.org/10.2514/3.63237
[32] H. Raposo, M. Azarpeyvand, Turbulence ingestion noise generation in rotating blades, J. Fluid Mech. 980 (2024) A53. https://doi.org/10.1017/jfm.2024.7
[33] J. Christophe, J. Anthoine, S. Moreau, Amiet'S theory in spanwise-varying flow conditions, AIAA J. 47 (3) (2009) 788–790. https://doi.org/doi.org/10.2514/1.37502
[34] A. Piccolo, R. Zamponi, F. Avallone, D. Ragni, Modification of Amiet's model for turbulence-ingestion noise prediction in rotors, J. Acoust. Soc. Am. 158 (1) (2025) 461–475. https://doi.org/10.1121/10.0037185
[35] F.L. Dos Santos, L. Botero-Bolívar, C.H. Venner, L.D. De Santana, Inflow turbulence distortion for airfoil leading-edge noise prediction for large turbulence length scales for zero-mean loading, J. Acoust. Soc. Am. 153 (3) (2023) 1811–1822. https://doi.org/10.1121/10.0017458
[36] A. Piccolo, R. Zamponi, F. Avallone, D. Ragni, Turbulence distortion and leading-edge noise, Phys. Fluids 36 (12) (2024). https://doi.org/10.1063/5.0244627
[37] A. Piccolo, R. Zamponi, F. Avallone, D. Ragni, Turbulence-distortion modelling for amiet's theory enhancement, J. Sound Vib. 624 (2026) 119503. https://doi.org/10.1016/j.jsv.2025.119503
[38] L.D. Santana, J. Christophe, C. Schram, W. Desmet, A rapid distortion theory modified turbulence spectra for semi-analytical airfoil noise prediction, J. Sound Vib. 383 (2016) 349–363. https://doi.org/10.1016/j.jsv.2016.07.026
[39] R.F. Miotto, W.R. Wolf, L.D. de Santana, Numerical computation of aeroacoustic transfer functions for realistic airfoils, J. Sound Vib. 407 (2017) 253–270. https://doi.org/10.1016/j.jsv.2017.06.037
[40] J. Hunt, A theory of turbulent flow round two-dimensional bluff bodies, J. Fluid Mech. 61 (4) (1973) 625–706. https://doi.org/10.1017/S0022112073000893
[41] S.T. Go, M.J. Kingan, L. Bowen, M. Azarpeyvand, Noise of a shrouded propeller due to ingestion of grid-generated turbulence, J. Sound Vib. 571 (2024) 118044.

[42] L. Trascinelli, G. Romani, L. Hanson, D. Casalino, B. Zang, B.Y. Zhou, M. Azarpeyvand, Numerical simulations of large-scale turbulence ingestion by a forward flight propeller, J. Acoust. Soc. Am. 158 (1) (2025) 826–837. https://doi.org/10.1121/10.0037219
[43] R. Zhang, X. Shan, H. Chen, Efficient kinetic method for fluid simulation beyond the navier-Stokes equation, Phys. Rev. E–Statist., Nonlinear, and Soft Matter Phys. 74 (4) (2006) 046703. https://doi.org/10.1103/PhysRevE.74.046703
[44] H. Chen, S. Kandasamy, S. Orszag, R. Shock, S. Succi, V. Yakhot, Extended boltzmann kinetic equation for turbulent flows, Science 301 (5633) (2003) 633–636. https://doi.org/10.1126/science.1085048
[45] H. Chen, S. Chen, W.H. Matthaeus, Recovery of the navier-Stokes equations using a lattice-gas boltzmann method, Phys. Rev. A 45 (8) (1992) R5339. https://doi.org/10.1103/PhysRevA.45.R5339
[46] J.P. Boris, F.F. Grinstein, E.S. Oran, R.L. Kolbe, New insights into large eddy simulation, Fluid Dyn. Res. 10 (4-6) (1992) 199. https://doi.org/10.1016/0169-5983(92)90023-P
[47] G. Romani, E. Grande, F. Avallone, D. Ragni, D. Casalino, Computational study of flow incidence effects on the aeroacoustics of low blade-tip mach number propellers, Aerosp. Sci. Technol. 120 (2022) 107275. https://doi.org/10.1016/j.ast.2021.107275
[48] S. Montagner, On the effects of freestream turbulence on a small drone propeller aerodynamics and aeroacoustics, 2024.
[49] P.E. Roach, The generation of nearly isotropic turbulence by means of grids, Int. J. Heat Fluid Flow 8 (2) (1987) 82–92. https://doi.org/10.1016/0142-727X(87)90001-4
[50] F. Farassat, Derivation of Formulations 1 and 1A of Farassat, Technical Report, 2007.
[51] D. Casalino, An advanced time approach for acoustic analogy predictions, J. Sound Vib. 261 (4) (2003) 583–612. https://doi.org/10.1016/S0022-460X(02)00986-0
[52] R. Zamponi, S. Satcunanathan, S. Moreau, D. Ragni, M. Meinke, W. Schröder, C. Schram, On the role of turbulence distortion on leading-edge noise reduction by means of porosity, J. Sound Vib. 485 (2020) 115561. https://doi.org/10.1016/j.jsv.2020.115561
[53] D. Casalino, F. Avallone, I. Gonzalez-Martino, D. Ragni, Aeroacoustic study of a wavy stator leading edge in a realistic fan/OGV stage, J. Sound Vib. 442 (2019) 138–154. https://doi.org/10.1016/j.jsv.2018.10.057
[54] J.H. Stephenson, D. Weitsman, N.S. Zawodny, Effects of flow recirculation on unmanned aircraft system (UAS) acoustic measurements in closed anechoic chambers, J. Acoust. Soc. Am. 145 (3) (2019) 1153–1155. https://doi.org/10.1121/1.5092213
[55] C. Nardari, D. Casalino, F. Polidoro, V. Coralic, P.-T. Lew, J. Brodie, Numerical and experimental investigation of flow confinement effects on UAV rotor noise, in: 25Th AIAA/CEAS Aeroacoustics Conference, 2019, p. 2497.
[56] F. Petricelli, P. Chaitanya, S. Palleja-Cabre, S. Meloni, P.F. Joseph, A. Karimian, S. Palani, R. Camussi, An experimental investigation on the effect of in-flow distortions of propeller noise, Appl. Acoust. 214 (2023) 109682.
[57] D. Sundararajan, Fourier Analysis–A Signal Processing Approach, 42, Springer, 2018.
[58] F. Avallone, S. Pröbsting, D. Ragni, Three-dimensional flow field over a trailing-edge serration and implications on broadband noise, Phys. Fluids 28 (11) (2016). https://doi.org/10.1063/1.4966633
[59] F.N. Frenkiel, The decay of isotropic turbulence (1948). https://doi.org/10.1115/1.4009853
[60] M.S. Uberoi, Effect of wind-tunnel contraction on free-stream turbulence, J. Aeronaut. Sci. 23 (8) (1956) 754–764. https://doi.org/doi.org/10.2514/8.3651
[61] G. McLelland, D. MacManus, C. Sheaf, The effect of streamtube contraction on the characteristics of a streamwise vortex, J. Fluids Eng. 137 (6) (2015) 061204. https://doi.org/10.1115/1.4029661
[62] R. Zamponi, S. Moreau, C. Schram, Rapid distortion theory of turbulent flow around a porous cylinder, J. Fluid Mech. 915 (2021) A27. https://doi.org/10.1017/jfm.2021.8
[63] K. Kücükcoskun, Prediction of free and scattered acoustic fields of low-speed fans, Ph.D. thesis, Ecole Centrale de Lyon; Institut von Karman de dynamique des fluides, 2012.